

RESOLVING THE RADIO SOURCE BACKGROUND: DEEPER UNDERSTANDING THROUGH CONFUSION

J. J. CONDON¹, W. D. COTTON¹, E. B. FOMALONT¹, AND K. I. KELLERMANN¹
National Radio Astronomy Observatory, 520 Edgemont Road, Charlottesville, VA 22903, USA

N. MILLER
Department of Astronomy, University of Maryland, College Park, MD 20742-2421, USA

R. A. PERLEY¹
National Radio Astronomy Observatory, P.O. Box 0, Socorro, NM 87801, USA

D. SCOTT, T. VERNSTROM, AND J. V. WALL
Department of Physics and Astronomy, University of British Columbia, Vancouver, BC V6T 1C1, Canada
Draft version November 27, 2024

ABSTRACT

We used the Karl G. Jansky Very Large Array (VLA) to image one primary beam area at 3 GHz with 8" FWHM resolution and $1.0 \mu\text{Jy beam}^{-1}$ rms noise near the pointing center. The $P(D)$ distribution from the central 10 arcmin of this confusion-limited image constrains the count of discrete sources in the $1 < S(\mu\text{Jy}) < 10$ range. At this level the brightness-weighted differential count $S^2 n(S)$ is converging rapidly, as predicted by evolutionary models in which the faintest radio sources are star-forming galaxies; and $\approx 96\%$ of the background originating in galaxies has been resolved into discrete sources. About 63% of the radio background is produced by AGNs, and the remaining 37% comes from star-forming galaxies that obey the far-infrared (FIR) / radio correlation and account for most of the FIR background at $\lambda \approx 160 \mu\text{m}$. Our new data confirm that radio sources powered by AGNs and star formation evolve at about the same rate, a result consistent with AGN feedback and the rough The confusion at centimeter wavelengths is low enough that neither the planned SKA nor its pathfinder ASKAP EMU survey should be confusion limited, and the ultimate source detection limit imposed by "natural" confusion is $\leq 0.01 \mu\text{Jy}$ at $\nu = 1.4$ GHz. If discrete sources dominate the bright extragalactic background reported by ARCADE 2 at 3.3 GHz, they cannot be located in or near galaxies and most are $\leq 0.03 \mu\text{Jy}$ at 1.4 GHz.

Subject headings: cosmology: diffuse radiation — cosmology: observations — galaxies: statistics — radio continuum: galaxies

1. INTRODUCTION

1.1. Counts of Extragalactic Radio Sources

Together the number per steradian $n(S)dS$ of discrete extragalactic radio sources having flux densities S to $S + dS$ and the brightness temperature T_b that sources contribute to the sky background constrain the nature and evolution of all extragalactic radio sources, even those too faint to be counted individually. Counts of radio sources achieved instant fame and notoriety with the announcement by Ryle (1955) and Ryle & Scheuer (1955) that the source count from the 2C survey was dramatically steeper than that expected for a uniformly-filled Euclidean universe. The remarkable Ryle & Scheuer (1955) paper claimed that the majority of "radio stars" were extragalactic, that they were so distant and radio-luminous as to be mostly beyond the reach of then-existing optical telescopes, and that the steep count showed dramatic cosmic evolution for individual objects in space density or luminosity. Then revolutionary, it remains a succinct

summary of our current understanding of extragalactic radio sources.

The claimed evolution sparked a bitter and public dispute, refuting as it did the popular steady-state cosmology (Bondi & Gold 1948; Hoyle 1948). Also the 2C radio source count was made before radio astronomers appreciated the importance of confusion and Eddington bias. Mills & Slee (1957) showed the great majority of the 2C sources were just "confusion bumps," the broad 2C beam often blending two or more faint background sources to appear as a single stronger source. Mills & Slee (1957) also noted that the count from their higher-resolution survey showed "no cosmological effects" with the possible exception of mild clustering. By that time, however, the Cambridge group had fully understood what went wrong, and the aftermath triggered (1) the 3C and 4C Cambridge surveys which were carefully cognizant of confusion, (2) the pioneering $P(D)$ analysis of confusion by Scheuer (1957) which showed how to extract the true source count from a confusion-limited survey, and (3) the first aperture-synthesis images (Ryle & Neville 1962) which revealed a decreased source-count slope (loosely termed "turnover") at flux densities below 1 Jy.

¹ The NRAO is a facility of the National Science Foundation operated by Associated Universities, Inc.

By 1966 there was general agreement about the counts of sources stronger than $S \sim 0.1$ Jy at low frequencies. The 4C confusion $P(D)$ (Hewish 1961) and direct (Gower 1966) counts had mapped their main features: a rise steeper than the static Euclidean slope followed by a decrease to sub-Euclidean slopes at flux densities below 1 Jy. Independent sky surveys, such as the Parkes survey (Bolton et al. 1964), were in agreement. To explain the source count, several investigators developed mathematical (non-physical) models for the cosmic evolution of extragalactic radio sources. Longair (1966) first showed that the relatively rapid change of the count slope could be explained by differential cosmic evolution, in which the more luminous sources underwent more evolution in their comoving space density than their less-luminous counterparts did.

Sensitive surveys made with the WSRT and VLA in the 1980s extended the 1.4 GHz source count down to mJy levels and below. Condon & Mitchell (1984) and Windhorst et al. (1985) discovered a point of inflection near 1 mJy below which the count slope flattens, suggesting the emergence of a new population of radio sources. Spiral galaxies dominate the local radio luminosity function below $L \sim 10^{23}$ W Hz⁻¹. Radio sources powered by star formation in spiral galaxies can account for this new population and for nearly half of the extragalactic sky background if they evolve at about the same rate as the stronger sources powered by active galactic nuclei (AGNs) in elliptical galaxies (Condon 1984a). Later models (Wall 1997; Boyle & Terlevich 1998; Wilman et al. 2008) find evolution similar to that of the cosmic star-formation rate shown in the Lilly-Madau diagram [see Hopkins (2007) for a modern data-set]. Massardi et al. (2010) accounted for the inflection with an evolutionary model using the empirical FIR/radio correlation, FIR counts, and the redshift distributions of star-forming galaxies. A recent compilation of source counts from surveys at frequencies 150 MHz to 15 GHz is presented by De Zotti et al. (2010); features and cosmic implications are discussed there in detail.

Of particular note in the present context are persistent discrepancies among the most sensitive 1.4 GHz direct counts that far exceed both Poisson and clustering uncertainties (Condon 2007; Owen & Morrison 2008). These discrepancies may result from different authors making different corrections for the effects of partial resolution. Resolution corrections can be large and difficult to estimate for an image whose resolution approaches the median angular size $\langle \theta_s \rangle \sim 1''$ of faint sources. The deep synthesis counts were also extended by confusion $P(D)$ distributions in low-resolution images (Mitchell & Condon 1985; Windhorst et al. 1993). We used their approach here to count sources a factor of ten fainter in a low-resolution (8'' FWHM) 3 GHz image that does not need significant corrections for partial resolution.

1.2. The Source Contribution Sky Brightness

The radio source count and the source contribution to the sky brightness at frequency ν are connected by the Rayleigh-Jeans approximation

$$S_n(S)dS = \frac{2k_B dT_b \nu^2}{c^2}, \quad (1)$$

where $k_B \approx 1.38 \times 10^{-23}$ J K⁻¹ is the Boltzmann constant and dT_b is the sky brightness temperature added by the $n(S)$ sources per steradian with flux densities S to $S + dS$. The observed source count now spans eight decades of flux density, so it must be plotted with a logarithmic abscissa. Substituting $d[\ln(S)] = dS/S$ gives the brightness temperature contribution per decade of flux density

$$\left[\frac{dT_b}{d \log(S)} \right] = \left[\frac{\ln(10)c^2}{2k_B \nu^2} \right] S^2 n(S). \quad (2)$$

The cumulative brightness temperature from all sources stronger than any detection limit S_0 is

$$\Delta T_b(> S_0) = \left[\frac{\ln(10)c^2}{2k_B \nu^2} \right] \int_{S_0}^{\infty} S^2 n(S) d[\log(S)]. \quad (3)$$

If S_0 is low enough, ΔT_b approaches the total T_b of the source background, and we can say that the background has been resolved into known sources. For example, Glenn et al. (2010) resolved about half of the far-infrared (FIR) background at $\lambda = 250, 350,$ and $500 \mu\text{m}$; and the Herschel/PEP (PACS Evolutionary Probe) survey (Berta et al. 2011) resolved about 3/4 of the COBE/DIRBE background at $\lambda = 160 \mu\text{m}$.

Figure 1 shows the flux-density range covered by published 1.4 GHz source counts. We plotted the weighted count $\log[S^2 n(S)]$ instead of the traditional Euclidean-weighted count $\log[S^{5/2} n(S)]$ as a function of $\log(S)$ because (1) $S^2 n(S)$ is proportional to the source contribution per decade of flux density to the sky temperature (Eq. 2), (2) the radio universe is neither static nor Euclidean, and (3) the plotted slopes are minimized for easy visual recognition of broad features, unlike the steeply sloped plot of $\log[n(S)]$ for example. On a plot of $\log[S^2 n(S)]$, the source count must ultimately fall off at both ends to avoid Olbers' paradox.

The filled points at $\log[S \text{ (Jy)}] > -3$ are from the many surveys referenced in Condon (1984a), and the filled data points at lower flux densities are from the Mitchell & Condon (1985) confusion-limited VLA survey. The irregular box encloses the range of 1.4 GHz counts consistent with the probability distribution $P(D)$ of confusion amplitudes D (in brightness units μJy per beam solid angle) in the low-resolution (17''5 FWHM) Mitchell & Condon (1985) image. The straight line inside the box indicates the best power-law fit to the $P(D)$ data. The open data points and their power-law fit (upper straight line) indicate the direct count of individual sources from the most sensitive high-resolution 1.4 GHz survey ever made with the original VLA (Owen & Morrison 2008). These two faint-source counts disagree by several times the Poisson counting errors, and nearly all other published faint-source counts are scattered over the wide gap between them (Condon 2007), as illustrated by Figure 11 in Owen & Morrison (2008). The sources contributing to the data plotted in Figure 1 show no sign of resolving the extragalactic background at 1.4 GHz because the power-law fits to $S^2 n(S)$ are still rising near the flux density limit $S_0 \sim 10 \mu\text{Jy}$.

The solid curve in Figure 1 shows the Condon (1984b) evolutionary model for the total source count at 1.4 GHz. In this model, the stronger radio sources are powered

primarily by AGNs of elliptical galaxies (dashed curve) and most of the fainter sources are in star-forming spiral galaxies (dotted curve). The model predicts that (1) $S^2n(S)$ should converge below $S \sim 10 \mu\text{Jy}$ and (2) most of the model's $T_b \approx 100 \text{ mK}$ background should be resolved into sources stronger than $S \sim 1 \mu\text{Jy}$.

However, Fixsen et al. (2011) reported that the recent ARCADE 2 (Absolute Radiometer for Cosmology, Astrophysics, and Diffuse Emission) balloon measurement of absolute sky brightness leaves a remarkably high extragalactic $T_b = 54 \pm 6 \text{ mK}$ at $\nu = 3.3 \text{ GHz}$ after the Galactic foreground and the $T = 2.731 \pm 0.004 \text{ K}$ cosmic microwave background (CMB) were subtracted. Combining their 3.3 GHz result with low-frequency data from the literature led Fixsen et al. (2011) to fit the “excess” extragalactic background with a power-law spectrum

$$T_b = (24.1 \pm 2.1 \text{ K}) \times \left(\frac{\nu}{310 \text{ MHz}} \right)^{-2.599 \pm 0.036} \quad (4)$$

between 22 MHz and 10 GHz. Equation 4 gives $T_b \approx 480 \text{ mK}$ at 1.4 GHz, almost five times the $T_b \approx 100 \text{ mK}$ predicted for the known populations of extragalactic sources.

With the goals of (1) determining an accurate source count down to $S \sim 1 \mu\text{Jy}$, (2) resolving the radio sky background contributed by galaxies, and (3) constraining possible source populations that could produce the high ARCADE 2 background at 3.3 GHz, we used the Karl G. Jansky Very Large Array (VLA) to make a very sensitive (rms noise $\sigma_n \approx 1 \mu\text{Jy beam}^{-1}$) low-resolution ($8''$ FWHM) confusion-limited sky image covering one primary beam area at S band (2–4 GHz). We pointed at the center of the “crowded” Owen & Morrison (2008) field to see if we could confirm the reported high source count there. Our relatively low angular resolution ensures that galaxy-size sources at cosmological distances are unresolved: $8''$ spans at least 40 kpc throughout the redshift range $0.4 < z < 7$ containing most faint radio sources. That low resolution also guarantees that the rms confusion is at least comparable with the rms noise, a necessary condition for using confusion to constrain the sky density of sources as faint as $S_0 \sim 1 \mu\text{Jy}$, which is more than a factor of five below our detection limit for individual sources.

1.3. Outline

Section 2 of this paper describes our observations and the production of a confusion-limited sky image. Section 3 presents the 3.02 GHz $P(D)$ distribution from the central region of this image. The 1.4 and 3.02 GHz source counts consistent with our $P(D)$ distribution are derived in Section 4, and the contributions of known extragalactic source populations to the sky brightness are discussed in Section 5. In Section 6 we use our narrow $P(D)$ distribution to show that the high ARCADE 2 background is too smooth to be produced by, or even spatially associated with, galaxies brighter than $m_{\text{AB}} = +29$. Section 7 summarizes our results.

2. OBSERVATIONS AND IMAGING

2.1. Target Field

We reobserved the “crowded” Owen & Morrison (2008) field centered on J2000 $\alpha = 10^{\text{h}} 46^{\text{m}} 00^{\text{s}}$, $\delta = +59^{\circ} 01' 00''$

over the 2–4 GHz S-band frequency range using an average of 21 antennas in the C configuration (maximum baseline length $\approx 3 \text{ km}$) of the VLA. This field in the Lockman Hole was originally selected by Owen & Morrison (2008) because it was covered by the *Spitzer* Wide-area InfraRed Extragalactic (SWIRE) legacy survey (Lonsdale et al. 2003), has exceptionally low infrared cirrus, and contains no strong radio sources. We favored it because it is far enough north to minimize S-band radio-frequency interference (RFI) from powerful geosynchronous broadcast satellites just south of the celestial equator and has the highest reported faint-source count (Owen & Morrison 2008).

2.2. Observations

Our 57 hours of observing time was divided among six observing nights between 2012 February 21 and March 18, and 50 hours of this time was spent integrating on the target field. The nearby unresolved phase calibrator J1035+564 was monitored for 30 seconds every 30 minutes. The flux density and bandpass calibrators 3C 147 and 3C 286 were each observed once per night. Antenna pointing accuracy was maintained with corrections determined from J1035+564 every hour. Accurate pointing is necessary even at S band because pointing errors can easily limit the dynamic range of an image filled with sources (Condon 2009).

The data-averaging period was 1 second of time, and the 2–4 GHz frequency range was divided into 16 correlator subbands, each with 64 spectral channels of width 2 MHz. The spectral resolution was broadened and the averaging intervals were increased somewhat prior to imaging, but both bandwidth and time smearing were always kept small enough that our sky coverage is limited only by the primary-beam attenuation of the individual 25 m antennas. Their attenuation pattern is very nearly that of a uniformly illuminated circular aperture (Condon et al. 1998):

$$A(\rho/\theta_p) \approx \left[\frac{2J_1(3.233\rho/\theta)}{(3.233\rho/\theta)} \right]^2, \quad (5)$$

where J_1 is the Bessel function of the first kind and order, ρ is the angular offset from the pointing center, and

$$\theta_p = (43'.3 \pm 0'.4) \left(\frac{\nu}{\text{GHz}} \right)^{-1} \quad (6)$$

is the measured full width between half-maximum points (FWHM) of the S-band primary beam at frequency ν . The primary FWHM ranges from 21'.7 at $\nu = 2 \text{ GHz}$ to 10'.8 at $\nu = 4 \text{ GHz}$.

2.3. Editing and Calibration

We used the Obit package (Cotton 2008)² to edit and calibrate the (u, v) data. The six observing sessions were calibrated and edited separately. Two of the 16 subbands contained satellite RFI strong enough to cause serious Gibbs ringing in the raw data, a consequence of the finite number of correlator lags. Hanning smoothing (combining adjacent spectral channels with weights 1/4, 1/2, and 1/4) suppressed this ringing and broadened

² <http://www.cv.nrao.edu/~bcotton/Obit.html>

the spectral resolution to about 4 MHz. The new VLA correlator was designed to prevent “bleeding” of ringing and other nonlinearities from one subband to another. Spectral channels still containing strong interfering signals were flagged and removed from the data, as were a few edge channels in each subband. Prior to calibration, the remaining data samples containing strong interfering signals that were impulsive in time or frequency were identified by their large deviations from running medians in time and frequency, and they were flagged. Calibrator observations were also subjected to a test of the RMS/mean amplitude ratios in each data stream, and noisy data segments with high RMS/mean amplitude ratios were deleted.

Subsequent calibration and editing consisted of the following steps:

1. Instrumental group delay offsets were determined from observations of 3C 147, 3C 286, and J1035+564 and applied to all of the data.
2. Residual variations of gain and phase with frequency were corrected by bandpass calibration based on 3C 286.
3. Amplitude calibration was based on the VLA standard spectrum of 3C 286 (see Table 1, column 3) bootstrapped to determine the spectrum of the astrometric calibrator J1035+564. The more frequent observations of J1035+564 were then used to calibrate the amplitudes and phases the target (u, v) data. Data from some antennas, time intervals, and frequency ranges were still degraded by interference that had evaded earlier editing and corrupted a small fraction of our amplitude and phase solutions. These corrupted solutions were detected by a comparison with all solutions, and data implying deviant complex gains were flagged.
4. The calibrated data were then subjected to further editing in which data with excessive Stokes I or V amplitudes were deleted, as well as another pass at removing narrowband interference.

After this calibration and editing, the initial calibration was reset and the whole process was repeated using only the data that had survived the editing process. Finally, because the target field contains no sources brighter than 5 mJy beam^{-1} , we were able to flag the small amount of the data having amplitudes significantly above the noise. About 53% of the (u, v) data survived all of the editing steps. The calibrated and edited (u, v) data from all six observing sessions were then combined for imaging.

2.4. Imaging

Observations spanning the frequency range between the low frequency limit ν_l and the high frequency limit ν_h have center frequency $\nu_c = (\nu_l + \nu_h)/2$, bandwidth $\Delta\nu = (\nu_h - \nu_l)$, and fractional bandwidth $\Delta\nu/\nu_c$. The fractional bandwidth covered by our 2–4 GHz (u, v) data is exceptionally large: $\Delta\nu/\nu_c = 2/3$. Using such data to make an image suitable for measuring confusion encounters three interesting problems—the field of view, the point-spread function (PSF), and the flux densities

of most sources can vary significantly with frequency. To deal with these problems, we separated the (u, v) data into 16 subbands each having a small fractional bandwidth $\Delta\nu/\nu_c \ll 1$. The (u, v) data were tapered heavily in the higher-frequency subbands, and each subband was imaged with an independent “robustness” (Briggs 1995) to force nearly identical PSFs in all subbands. We weighted and recombined the narrowband images to produce a sensitive wideband image characterized by an “effective frequency” $\langle\nu\rangle$, where $\langle\nu\rangle$ at any position in a wideband image is defined as the frequency at which the flux density of a point source with a typical spectral index $\langle\alpha\rangle \equiv d \ln S / d \ln \nu = -0.7$ equals its flux density in the wideband sky image. The effective frequency declines with angular distance ρ from the pointing center because the primary beamwidth is inversely proportional to frequency.

Table 1 lists the center frequencies ν_c of the 16 subbands and the rms noise values σ_n of the 16 subband images. The fractional bandwidths of these subbands range from 3% to 6%, so each subband image is a narrowband image. We used the Observe task MFImage to form separate dirty and residual images in each subband. We assigned each subband image a weight inversely proportional to its rms noise, generated a combined wideband image from their weighted average, and used this sensitive combined image to locate CLEAN components for a joint deconvolution. The CLEAN operation used flux densities from the individual subband images but at locations selected from the combined image. At the end of each major CLEAN cycle, the CLEAN components with flux densities from the individual subband images were used to create residual subband (u, v) data and then new residual images.

The effects of sky curvature across the field of view were eliminated by faceted “fly’s eye” imaging in which each facet was small enough to make the curvature effects negligible. Each facet image was projected onto a common coordinate grid on one tangent plane to form a single continuous central image 30 arcmin in radius. This allowed all facets to be CLEANed in parallel. Outside the central image, separate outlier facets were added at the positions of those NVSS (Condon et al. 1998) sources whose uncleaned sidelobes might otherwise affect our target field. Before imaging, the data were averaged over baseline-dependent time intervals subject to the constraints that (1) the averaging should not cause time smearing within our central image and (2) the averaging time should never exceed the 20 second phase self-calibration interval.

In order to obtain nearly identical PSFs in all subbands, we tapered the (u, v) data in each subband differently and assigned individual “robust” weighting factors adjusted to ensure that each synthesized “dirty” beam was nearly circular with major and minor axes between $7''$ and $8''$. After CLEANing, each residual image was smoothed by convolution with its own elliptical Gaussian tailored to yield a circular and nearly Gaussian PSF with a precisely $8''$ FWHM. Having the same dirty beam and PSF in each subband image is critical for an accurate confusion analysis because only those sources much stronger than the rms confusion were actually CLEANed. Finally, all CLEAN components were restored with an $8''$ FWHM circular Gaussian beam.

Two iterations of phase-only self calibration were used to remove residual atmospheric phase fluctuations. The final CLEAN cycle was stopped when the peak in the combined residual image reached $10 \mu\text{Jy beam}^{-1}$, a level well above the rms noise and confusion in the combined image. The total CLEANed flux density in the combined image is 21 mJy .

Unwanted fluctuations indistinguishable from confusion are produced by any dirty-beam sidelobes remaining in our combined image. Fortunately, they are small because the combination of long observing tracks and bandwidth synthesis over our wide fractional bandwidth ensures excellent (u, v) -plane coverage and keeps the dirty-beam sidelobe levels well below 1% of the peak, as shown in Figure 2. Consequently the highest dirty-beam sidelobes from sources in the residual image are $< 0.01 \times 10 \mu\text{Jy beam}^{-1} \approx 0.1 \mu\text{Jy beam}^{-1}$, so their contribution to the image variance is more than two orders of magnitude below the $\sim (1 \mu\text{Jy beam}^{-1})^2$ contributions of noise and confusion.

We used the AIPS task IMEAN to calculate the rms noise values σ_n of the CLEANed subband images in several large areas that are well outside the main lobe of the primary beam and contain no visible ($S_p \gtrsim 6 \mu\text{Jy beam}^{-1}$) sources; the σ_n are listed in Table 1. Next we assigned to each subband image a weight inversely proportional to its noise variance σ_n^2 , generated a wideband image from the weighted average of the subband images, and measured the noise distribution in four large regions well outside the primary main beam and free of visible sources. Figure 3 shows a logarithmic histogram of the noise amplitudes in one such region covering an area $\Omega = N\Omega_b$ containing $N \approx 4000$ synthesized beam solid angles $\Omega_b \equiv \pi\theta_s^2/(4 \ln 2) \approx 0.020 \text{ arcmin}^2$ for $\theta_s = 8''$. The excellent parabolic fit to the logarithmic histogram indicates a precisely Gaussian noise amplitude distribution with an rms $\sigma_n \approx 1.02 \mu\text{Jy beam}^{-1}$.

What is the rms statistical uncertainty $\Delta\sigma_n$ in our estimate of σ_n ? The image PSF is a Gaussian, and the effective noise area for a Gaussian PSF is that of the Gaussian PSF squared (Condon 1997; Condon et al. 1998). Squaring a Gaussian PSF of width θ yields a narrower Gaussian of width $2^{-1/2}\theta$ and solid angle $\Omega_b/2$. Consequently there are actually $2N$ statistically independent noise samples in $\Omega = N\Omega_b$ beam solid angles, and the rms fractional uncertainty in σ_n is

$$\frac{\Delta\sigma_n}{\sigma_n} = \left(\frac{1}{2N} \right)^{1/2}, \quad (7)$$

not the commonly believed $(1/N)^{1/2}$. See the Appendix for a detailed derivation of equation 7.

The final result from the four areas covering a total $N = 11570$ beam solid angles is $\sigma_n = 1.012 \pm 0.007 \mu\text{Jy beam}^{-1}$ (statistical error only). In theory the rms noise is uniform across the image prior to correction for primary-beam attenuation, so we used this value to estimate the noise in confusion-limited regions near the pointing center. The total intensity-proportional error arising from uncertainties in the flux-density calibration and primary beamwidth is not more than 3% inside the primary beam half-power circle.

2.5. The SNR-Optimized Wideband Sky Image

Our final wideband image of the sky was made with weights designed to correct for primary-beam attenuation and simultaneously maximize the signal-to-noise ratio (SNR) for sources having spectral indices near $\langle\alpha\rangle = -0.7$, the mean spectral index of faint sources found at frequencies around 3 GHz (Condon 1984b). This differs from the traditional weighting designed to minimize noise, which maximizes the SNR in a narrowband image, but in a wideband image only if $\langle\alpha\rangle \approx 0$. The brightness $b_i(\rho)$ of each pixel in each of the $i = 1, 16$ subband images was assigned a weight

$$W_i(\rho, \nu_c) \propto \left[\frac{\nu_c^{\langle\alpha\rangle}}{\sigma_n A(\rho, \nu_c)} \right]^2, \quad (8)$$

where the rms noise σ_n and center frequency ν_c of each subband image is listed in Table 1. Each pixel in the weighted wideband sky image was generated from the ratio

$$b(\rho) = \frac{\sum_{i=1}^{16} [b_i(\rho)W_i(\rho)]}{\sum_{i=1}^{16} W_i(\rho)} \quad (9)$$

Even at the pointing center, weighting to optimize the SNR for $\langle\alpha\rangle = -0.7$ increases the sky image noise slightly from $\sigma_n = 1.012 \pm 0.007 \mu\text{Jy beam}^{-1}$ to $\sigma_n = 1.080 \pm 0.007 \mu\text{Jy beam}^{-1}$. Away from the pointing center, the frequency-dependent primary-beam attenuation correction causes the rms noise on the sky image to grow with the radial offset ρ at the rate indicated by the dashed curve in Figure 4. Weighting also affects how the effective frequency $\langle\nu\rangle$ at each point in the wideband sky image decreases with the offset ρ from the pointing center. The dashed curve in Figure 5 indicates how $\langle\nu\rangle$ in our sky image declines monotonically from 3.06 GHz at the pointing center to 2.96 GHz at $\rho = 5 \text{ arcmin}$.

Figure 6 is a profile plot of the central portion of our SNR-optimized wideband sky image. The intensity scale can be inferred from the highest peaks, which are truncated at $S_p = 100 \mu\text{Jy beam}^{-1}$. This image is confusion limited in the sense that the rms fluctuations are everywhere larger than the noise levels plotted in Figure 4.

3. THE $P(D)$ DISTRIBUTION

Historically, confusion was measured from the probability distribution $P(D)$ of pen deflections D on a chart-recorder plot of fringe amplitudes from the single baseline of a two-element radio interferometer (Scheuer 1957). On a single-dish or aperture-synthesis array image, the corresponding “deflection” D at any pixel is the intensity in units of flux density per beam solid angle. The observed D at any point is the sum of the contribution from the noise-free source confusion and the contribution from image noise. The source confusion and noise contributions are independent of each other, so the the observed $P(D)$ distribution is the convolution of the source confusion and noise distributions, and the variance σ_o^2 of the observed $P(D)$ distribution is the sum of variances of the noise-free source confusion (σ_c^2) and the noise (σ_n^2) distributions:

$$\sigma_o^2 = \sigma_c^2 + \sigma_n^2. \quad (10)$$

The goal is to extract the source confusion distribution and its width

$$\sigma_c = (\sigma_o^2 - \sigma_n^2)^{1/2} \quad (11)$$

from the observed deflections and the measured noise. If $\sigma_c \ll \sigma_n$, then $\partial\sigma_c/\partial\sigma_o \approx (\sigma_o/\sigma_c) \approx (\sigma_n/\sigma_c) \gg 1$ and small errors in the measured σ_o (or σ_n) cause large errors in the extracted σ_c . This is the reason that only fairly low-resolution ($\sigma_c > \sigma_n$) images can be used to measure confusion. Also, to the extent that other sources of error (e.g., uncleaned sidelobes) are present but not accounted for, equation 11 will tend to overestimate the source confusion.

The noise in our weighted sky image is low at the center but increases with radial distance ρ from the pointing center, and the noise eventually overwhelms the confusion at large ρ . On the other hand, increasing the radius ρ of the circular region inside which the $P(D)$ distribution is measured increases the number N of beam solid angles sampled and thus acts to decrease the statistical uncertainty $\Delta\sigma_o$ in the width of the observed $P(D)$ distribution. For each thin ring of radius ρ covering N beam solid angles, we use equation 10 to calculate

$$(\Delta\sigma_o)^2 = \left(\frac{\partial\sigma_o}{\partial\sigma_c}\Delta\sigma_c\right)^2 + \left(\frac{\partial\sigma_o}{\partial\sigma_n}\Delta\sigma_n\right)^2, \quad (12)$$

where

$$\frac{\partial\sigma_o}{\partial\sigma_c} = \frac{\sigma_c}{\sigma_o} \quad \text{and} \quad \frac{\partial\sigma_o}{\partial\sigma_n} = \frac{\sigma_n}{\sigma_o}. \quad (13)$$

Then

$$\left(\frac{\Delta\sigma_o}{\sigma_o}\right)^2 = \frac{1}{\sigma_o^4} \left[\sigma_c^4 \left(\frac{\Delta\sigma_c}{\sigma_c}\right)^2 + \sigma_n^4 \left(\frac{\Delta\sigma_n}{\sigma_n}\right)^2 \right], \quad (14)$$

where $(\Delta\sigma_c/\sigma_c) \sim N^{-1/2}$ and $(\Delta\sigma_n/\sigma_n) = (2N)^{-1/2}$ (Eq. 7). In the limit $\sigma_n \gg \sigma_c$,

$$\left(\frac{\Delta\sigma_o}{\sigma_o}\right)^2 \approx \left(\frac{1}{2N\sigma_o^4}\right)\sigma_n^4. \quad (15)$$

To minimize the uncertainty σ_o inside the circle of radius ρ , we counted each pixel σ_n^{-4} times and truncated the count at $\rho \approx 5$ arcmin, where $\Delta\sigma_o/\sigma_o$ in the enclosed circle has a broad minimum. Within the circle of radius $\rho = 5$ arcmin, our weighted $P(D)$ distribution has rms noise $\sigma_n = 1.255 \mu\text{Jy beam}^{-1}$ (Fig. 4) and its effective frequency is $\langle\nu\rangle \approx 3.02$ GHz (Fig. 5).

The weighted $P(D)$ distribution within 5 arcmin of the pointing center is shown by the data points with their Poisson rms error bars in Figure 7. The thin curve indicates the Gaussian noise distribution with rms width $\sigma_n = 1.255 \mu\text{Jy beam}^{-1}$. Interferometers have no DC response to smooth emission, so the mean deflection $\langle D \rangle \approx 3 \mu\text{Jy beam}^{-1}$ in our image approximately equals the total CLEANed flux density divided by the number of beam solid angles in the image. Consequently, the image zero-point $D = 0$ should be treated as a free parameter when comparing the observed $P(D)$ distribution with analytic models of the true sky $P(D)$ distribution.

The noise-free confusion $P(D)$ distribution can be calculated analytically for the scale-free case of a power-law differential source count (Condon 1974)

$$n(S) = kS^{-\gamma}, \quad (16)$$

where k is the count normalization and $1 < \gamma < 3$ is the differential count slope. The shape of the noise-free $P(D)$ distribution depends only on γ , and the width of the noise-free $P(D)$ distribution obeys the scaling relation

$$P[(k\Omega_e)^{1/(\gamma-1)}D] = (k\Omega_e)^{-1/(\gamma-1)}P(D), \quad (17)$$

where Ω_e is the effective beam solid angle. If G is the normalized ($G = 1$ at the peak) PSF, then

$$\Omega_e = \int G^{\gamma-1} d\Omega \quad (18)$$

and

$$\Omega_e = \frac{\Omega_b}{\gamma-1} \quad (19)$$

for a circular Gaussian PSF. Equation 18 also implies that sidelobes of the PSF have a bigger effect as γ declines, so images suitable for confusion studies at sub- μJy levels, where $\gamma - 1 \sim 0.5$, need to have very low sidelobe levels. The rms confusion σ_c contributed by deflections fainter than some limiting signal-to-noise ratio $q = S_0/\sigma_c$ is (Condon 1974)

$$\sigma = \left(\frac{q^{3-\gamma}}{3-\gamma}\right)^{1/(\gamma-1)} (k\Omega_e)^{1/(\gamma-1)}. \quad (20)$$

If the number of sources per steradian stronger than S is

$$N(> S_0) = \int_{S_0}^{\infty} n(S) dS \quad (21)$$

then there are

$$\beta \equiv [N(> S_0)\Omega_b]^{-1} \quad (22)$$

beam solid angles per source stronger than S_0 . For a power-law source count,

$$\beta = \frac{q^2}{3-\gamma}. \quad (23)$$

Taking $q = 5$ for reliable source detection (Murdoch et al. 1973) and $\gamma \approx 2$, equation 20 limits the maximum density of reliably detectable and individually countable sources to about one source per 25 beam areas if $\gamma \sim 2$.

These equations apply to unresolved sources. The response to an extended source is the convolution of the source brightness distribution with the point-source response, and areas add under convolution. The integrated flux density is conserved, so the peak flux density falls. In the limit of a slightly resolved source covering a solid angle $\Omega_s \ll \Omega_e$, the peak flux density will be multiplied by the factor

$$f \approx \frac{\Omega_e}{\Omega_e + \Omega_s} \lesssim 1 \quad (24)$$

and the solid angle of the source response on the image will be divided by f . Thus equation 17 can be used to show that slightly extended sources multiply the width of the $P(D)$ distribution by

$$f^{(\gamma-2)/(\gamma-1)}. \quad (25)$$

The thick curve in Figure 7 is the convolution of the $\sigma_n = 1.255 \mu\text{Jy beam}^{-1}$ noise Gaussian with the noise-free $P(D)$ distribution for the power-law source count

$n(S) = 9000S^{-1.7} \text{ Jy}^{-1} \text{ sr}^{-1}$ of point sources and an $8''$ FWHM Gaussian PSF. Even if faint sources are as large as $\langle\theta_s\rangle \approx 1''.5$ (Owen & Morrison 2008), equation 25 indicates that the width of the $P(D)$ distribution would increase by less than 2%. Thus the source count based on our low-resolution $P(D)$ data should be much less sensitive to the angular-size distribution of faint sources than direct source counts from images that must have synthesized beam solid angles about 25 times smaller to reach the same flux-density limit.

4. SOURCE COUNTS AT 1.40 AND 3.02 GHz

To compare our 3.02 GHz $P(D)$ distribution with source counts at 1.4 GHz, we assume that the average spectral index between 1.4 and 3.02 GHz is $\langle\alpha\rangle = -0.7$, the value that best fits multifrequency counts of stronger sources (Condon 1984b). The power-law count $k_1 S^{-\gamma}$ at $\nu_1 = 1.4$ GHz can be converted to the count $k_2 S^{-\gamma}$ at $\nu_2 = 3.02$ GHz via the relation

$$\left(\frac{k_1}{k_2}\right) = \left(\frac{\nu_1}{\nu_2}\right)^{\langle\alpha\rangle(\gamma-1)} \quad (26)$$

If our estimate of $\langle\alpha\rangle$ is in error by 0.05 and $\gamma = 1.7$, the frequency conversion will cause an $\approx 3\%$ error in the calculated value of k_2 .

To span the range of faint-source counts reported at 1.4 GHz, we converted the relatively low Mitchell & Condon (1985) count $n(S) = 57S^{-2.2} \text{ Jy}^{-1} \text{ sr}^{-1}$ and the relatively high Owen & Morrison (2008) count $n(S) = 6S^{-2.5} \text{ Jy}^{-1} \text{ sr}^{-1}$ at $\nu_1 = 1.4$ GHz to counts at $\nu_2 = 3.02$ GHz and extrapolated them to lower flux densities. The noise-free 3.02 GHz $P(D)$ distributions for these counts observed with a $\theta = 8''$ FWHM Gaussian beam were convolved with the $\sigma_n = 1.255 \mu\text{Jy beam}^{-1}$ Gaussian noise distribution for comparison with the observed $P(D)$ distribution (Figure 8). The continuous curve is slightly lower and broader than the $P(D)$ data, indicating that the extrapolated Mitchell & Condon (1985) count is somewhat high, as expected from the rapidly converging weighted count $S^2 n(S)$ of the Condon (1984b) model. The dashed curve is much lower and broader because the extrapolated Owen & Morrison (2008) count is much higher.

Next we compared our 3.02 GHz $P(D)$ distribution with the predictions of two 1.4 GHz evolution models:

(1) The very simple Condon (1984b) model is based on old local 1.4 GHz luminosity functions derived from optically selected samples of elliptical galaxies (Auremma et al. 1977) and spiral galaxies (Hummel 1980). The radio sources in elliptical and spiral galaxies are primarily associated with AGNs and star formation, respectively, so these luminosity functions are similar to more modern luminosity functions in which the FIR/radio correlation and/or optical line spectra are used to distinguish radio sources primarily powered by AGN from those primarily powered by recently formed stars (Condon et al. 2002; Mauch & Sadler 2007). There were only sparse redshift data for identifications of strong radio sources, and a pre-WMAP cosmology was assumed. The decision to evolve both the AGN and star-forming source populations identically to match the source count at several frequencies was based on applying Occam’s razor to limited source-count data below $S \sim 1$ mJy, and not any

physical theory.

(2) The far more sophisticated and modern Wilman et al. (2008) semi-empirical simulation of the sky was made as part of the Square Kilometer Array Design Study (SKADS). It uses new and better local luminosity functions, redshift data, and a concordance cosmological model incorporating dark matter and dark energy.

Remarkably, both models predict nearly identical source counts all the way down to $S \sim 10$ nJy, and both agree well with our observed $P(D)$ distribution. This good agreement suggests that there is little “wiggle room” for models describing the counts of faint sources once the local radio luminosity function has been specified; the details of the evolution and the underlying cosmology seem to have little effect on the resulting source count (Condon 1989). The fact that our $P(D)$ count matches so well the $S^2 n(S)$ convergence below $S \approx 10 \mu\text{Jy}$ predicted by the Condon (1984b) and Wilman et al. (2008) models provides independent support for the claim that most faint radio sources are in star-forming galaxies. Such radio sources are usually somewhat smaller than their optical host galaxies, so we expect that the median angular diameter of μJy sources is $\theta_s \leq 1''$.

In the flux-density range $1 \lesssim S \lesssim 10 \mu\text{Jy}$, the 1.4 GHz model counts can be approximated by the power laws $n(S) = 1.2 \times 10^5 S^{-1.5} \text{ Jy}^{-1} \text{ sr}^{-1}$ (Condon 1984b) and $n(S) = 3.45 \times 10^4 S^{-1.6} \text{ Jy}^{-1} \text{ sr}^{-1}$ (Wilman et al. 2008). At 3.02 GHz these counts become $n(S) = 9.17 \times 10^4 S^{-1.5} \text{ Jy}^{-1} \text{ sr}^{-1}$ and $n(S) = 2.5 \times 10^4 S^{-1.6} \text{ Jy}^{-1} \text{ sr}^{-1}$, respectively, if $\langle\alpha\rangle = -0.7$. Figure 9 compares the Condon (1984b) (dashed curve) and Wilman et al. (2008) (continuous curve) model $P(D)$ distributions, after conversion to 3.02 GHz with $\langle\alpha\rangle = -0.7$ and convolution with $\sigma_n = 1.255 \mu\text{Jy beam}^{-1}$ noise, with the 3.02 GHz $P(D)$ data.

Although the power-law approximations to both models appear to agree fairly well with the $P(D)$ data in Figure 9, the normalized χ_ν^2 values from fits between $D = -3.9 \mu\text{Jy beam}^{-1}$ and $D = +9.7 \mu\text{Jy beam}^{-1}$ ($\nu = 66$ degrees of freedom) are too high: $\chi_\nu^2 \sim 100$ for the power-law approximation to the Condon (1984b) model and ~ 10 for the power-law approximation to the Wilman et al. (2008) model. Both approximations significantly overestimate the numbers of sources stronger than about $5 \mu\text{Jy}$. The $P(D)$ data are simply not consistent with *any* power-law approximation to the source count over the whole range $1 \lesssim D(\mu\text{Jy beam}^{-1}) \lesssim 10$. The best-fit slope at the high end of this range is $\gamma \approx 1.7$ while the best-fit slope at the low end is $\gamma \approx 1.5$. Better modeling of the source counts will require numerical simulations to generate $P(D)$ distributions for non-power-law source counts. The range of 3.02 GHz power-law counts reasonably consistent with the $P(D)$ data is spanned by the three fits already mentioned: $n(S) = 9.17 \times 10^4 S^{-1.5} \text{ Jy}^{-1} \text{ sr}^{-1}$ (Condon 1984b), $n(S) = 2.5 \times 10^4 S^{-1.6} \text{ Jy}^{-1} \text{ sr}^{-1}$ (Wilman et al. 2008), and $n(S) = 9000 S^{-1.7} \text{ Jy}^{-1} \text{ sr}^{-1}$ (Fig. 7).

4.1. The Noise-Free RMS Confusion

The corresponding noise-free $P(D)$ distributions for a $\theta = 8''$ FWHM Gaussian PSF are plotted in Figure 10.

Note that the zero-point deflection $D = 0$ in these calculated $P(D)$ distributions is the absolute zero of sky brightness contributed by discrete sources. For values of $\gamma \leq 1.7$, all sources fainter than $S \sim 1 \mu\text{Jy}$ contribute very little to the sky background. The rms confusion σ_c is a poor statistic for describing such skewed $P(D)$ distributions. In a Gaussian distribution, about 2/3 of the points lie within $\pm 1\sigma$ of the mean, so we use σ_c^* defined as half the range of D containing 2/3 of the points as a more stable measure of the width of the confusion distribution. In a $\theta = 8''$ FWHM PSF, this width of the noiseless confusion distribution is $\sigma_c^* \approx 1.2 \mu\text{Jy beam}^{-1}$ at $\nu = 3.02 \text{ GHz}$. For nearby values of θ and ν , the scaling equation 20 with $\gamma \approx 1.6$ implies

$$\sigma_c^* \approx 1.2 \mu\text{Jy beam}^{-1} \left(\frac{\nu}{3.02 \text{ GHz}} \right)^{-0.7} \left(\frac{\theta}{8''} \right)^{10/3}. \quad (27)$$

For example, the proposed EMU (Extragalactic Map of the Universe) survey will cover most of the sky at $\nu = 1.3 \text{ GHz}$ with $\theta = 10''$ resolution (Norris et al. 2011) and rms noise $\sigma_n = 10 \mu\text{Jy beam}^{-1}$. Equation 27 indicates that EMU will not be confusion limited, with $\sigma_c^* \approx 5 \mu\text{Jy beam}^{-1}$.

4.2. The Natural Confusion Limit

In addition to the instrumental confusion limit caused by finite angular resolution, there is a “natural” confusion limit caused by the finite angular size of faint sources. If the median solid angle covered by a faint source is $\langle \Omega_s \rangle$, then equations 22 and 23 imply the number of source solid angles per detectable source ($q > 5$) must exceed

$$\beta = [N(> S)\Omega_s] = \frac{q^2}{3 - \gamma} \sim 25 \quad (28)$$

even if the instrumental resolution is very high. Their high source count prompted Owen & Morrison (2008) to speculate that the natural confusion limit could be as high as $1 \mu\text{Jy}$, but our lower $P(D)$ count suggests that the natural confusion limit for detecting individual $\langle \Omega_s \rangle \sim (1'')^2$ sources is under 10 nJy . This is well below the hoped-for $5\sigma_n = 45 \text{ nJy}$ sensitivity limit of the full $12000 \text{ m}^2 \text{ K}^{-1}$ Square Kilometre Array (SKA) after 1 megasecond of integration, so the SKA continuum sensitivity should not be limited by either natural or instrumental confusion, but only by instrumental noise and dynamic range (Condon 2009).

4.3. The 1.4 GHz Source Count

The full range of 1.4 GHz source count data is plotted with the traditional $S^{5/2}n(S)$ “static Euclidean” normalization in Figure 11 for direct comparison with most published results. The range of 1.4 GHz source counts consistent with our $P(D)$ distribution is conservatively within the box covering $2 \lesssim S \lesssim 20 \mu\text{Jy}$. Again, obtaining more precise constraints on the counts consistent with our $P(D)$ distribution will require numerical simulations of non-power-law counts.

The upper abscissa of Figure 11 shows the source-frame 1.4 GHz spectral luminosity $L(\text{W Hz}^{-1})$ of a normal-spectrum ($\alpha \approx -0.7$) source whose flux density is directly below on the lower abscissa if the source is at the

median redshift $\langle z \rangle \sim 0.8$ of extragalactic sources (Condon 1989). These typical luminosities and flux densities at $z \sim 0.8$ can be compared with those of nearby radio sources such as the Large Magellanic Cloud (LMC) at $\log(L) \approx 20.3$ (Hughes et al. 2007) and $\log(S) \approx -7.1$, our own Galaxy at $\log(L) \approx 21.4$ (Berkhuijsen 1984) and $\log(S) \approx -6.0$, M82 at $\log(L) \approx 22.1$ (Kellermann et al. 1969) and $\log(S) \approx -5.3$, and Arp 220 at $\log(L) \approx 23.4$ (Condon et al. 2002) and $\log(S) \approx -4.0$. Most of the extragalactic radio sources fainter than our $P(D)$ limit were no more luminous at $z \sim 0.8$ than our Galaxy is today. For the first time, the count data are deep enough to confirm the assumption (Condon 1984a,b) that radio sources powered by AGNs and radio sources powered by star formation evolve at about the same rate. That assumption had no known physical justification in 1984, but it is consistent with the correlation between black hole and stellar bulge masses (Magorrian et al. 1998) discovered later. Note that this correlation appears to be weaker for the lower-mass ($\sim 10^7 M_\odot$) black holes found in late-type star-forming galaxies (Greene et al. 2010). The processes that produced the correlation for massive elliptical galaxies do not appear to have had enough time to fully establish the correlation for the star-forming galaxies that host most faint radio sources.

Our new source count is about a factor of four lower than the Owen & Morrison (2008) count near $S = 15 \mu\text{Jy}$, even though our fields overlap on the sky. What might cause this discrepancy and, for that matter, the surprisingly large scatter among all published faint-source counts (Condon 2007)? Are most of the faint Owen & Morrison (2008) sources spurious, or did we miss a large fraction of real sources that Owen & Morrison (2008) counted? The Owen & Morrison (2008) image has $\theta = 1''.6$ angular resolution, much higher than our $\theta = 8''$ resolution and the Mitchell & Condon (1985) $\theta = 17''.5$ resolution. How often have we blended into one “source” what Owen & Morrison (2008) resolved into two or more sources? Figure 12 shows our 3 GHz sky image as a gray scale with white crosses on the positions of cataloged Owen & Morrison (2008) sources stronger than $15 \mu\text{Jy}$ at 1.4 GHz. The correspondence is actually quite good. Almost all crosses have 3 GHz counterparts, and most of the brighter 3 GHz sources have 1.4 GHz counterparts, so spurious or missing sources cannot explain a factor of four discrepancy. Likewise, there are only a few cases of two Owen & Morrison (2008) sources blending into one source on our low-resolution image. We suspect that most of the count difference is caused by count corrections made for partial resolution of extended sources in the high-resolution 1.4 GHz beam. Survey catalogs are complete to a fixed brightness ($\mu\text{Jy beam}^{-1}$) cutoff, so extended sources with lower brightnesses but higher integrated flux densities (μJy) will be missed. The corrections needed to convert source brightnesses in $\mu\text{Jy beam}^{-1}$ to source flux densities in μJy and to account for missing sources become quite large near the brightness cutoff as the angular resolution approaches the median angular size of faint sources. For example, Owen & Morrison (2008) found a median angular size $\langle \phi \rangle = 1''.5$ in their 20–30 μJy bin, which is about the same as their FWHM resolution $\theta = 1''.6$. The rapid rise in counts near cutoffs at 6, 7, 8, 9, and 10 times the rms noise shown in Figure 9 of Owen & Morri-

son (2008) may be a sign that these corrections were too large.

5. THE CONTRIBUTIONS OF KNOWN SOURCES TO THE SKY BRIGHTNESS

The 1.4 GHz source counts in Figure 11 were replotted as $\log[S^2n(S)]$ versus $\log(S)$ in Figure 13 to emphasize the source contribution to sky brightness. The right ordinate of the top panel in Figure 13 shows the differential contribution $dT_b/d[\log(S)]$ to the 1.4 GHz sky brightness temperature per decade of flux density. The constraint provided by the new $P(D)$ distribution clearly shows that $S^2n(S)$ is falling off at low flux densities, at about the rate predicted by the Condon (1984b) and Wilman et al. (2008) evolutionary models.

We estimated the 1.4 GHz and 3.02 GHz backgrounds from the known source populations powered by AGNs and star-forming galaxies by inserting the 1.4 GHz source counts indicated by the solid curve in the top panel of Figure 13 into equation 3 and assuming an effective spectral index $\langle\alpha\rangle = -0.7$. The results are shown in the middle and bottom panels, respectively. The total background from the model sources converges to $T_b \approx 100$ mK at 1.4 GHz and $T_b \approx 13$ mK at 3.02 GHz. AGNs account for about 63% and star-forming galaxies 37% of the extragalactic source background. Approximately 96% of this total has been resolved into sources stronger than $S_0 \approx 2 \mu\text{Jy}$ at 1.4 GHz or $S_0 \approx 1 \mu\text{Jy}$ at 3.02 GHz. More specifically, nearly 100% of the AGN background and about 89% of the star-forming galaxy contribution to the background has been resolved.

Star-forming galaxies appear to obey the local FIR/radio correlation even at moderate redshifts $z \lesssim 2$ (Ivison et al. 2010), while the radio sources powered by AGNs have much lower FIR/radio flux ratios. Local ($z \ll 1$) star-forming galaxies have a mean FIR/radio flux ratio $\langle q \rangle \equiv \log[S(80 \mu\text{m})/S(1.4 \text{ GHz})] \approx 2.3$ (Condon 1992). Our claim that star-forming galaxies produce a $T_b \approx 37$ mK background at $\nu = 1.4$ GHz (equivalently, $I_\nu \sim 2.2 \times 10^{-23} \text{ W m}^{-2} \text{ Hz}^{-1} \text{ sr}^{-1}$) can be checked by comparison with the measured extragalactic FIR background. Fixsen et al. (1998) and Lagache et al. (1999) analyzed COBE FIRAS data to find $\nu I_\nu = 13.7 \pm 4 \text{ nW m}^{-2} \text{ sr}^{-1}$ at $\lambda = 160 \mu\text{m}$, or $I_\nu \approx 7.3 \times 10^{-21} \text{ W m}^{-2} \text{ Hz}^{-1} \text{ sr}^{-1}$ at $\nu \approx 1870$ GHz. Thus the background FIR/radio ratio is $q_b \equiv \log[I_\nu(160 \mu\text{m})/I_\nu(1.4 \text{ GHz})] \approx 2.5$. If the star-forming background galaxies have typical redshifts $\langle z \rangle \sim 0.8$ and radio spectral indices $\alpha \approx -0.7$, then these backgrounds imply that their source-frame FIR/radio ratio is $\log[S(90 \mu\text{m})/S(2.5 \text{ GHz})] \approx 2.5$, which corresponds to a source-frame FIR/radio flux ratio $\log[S(90 \mu\text{m})/S(1.4 \text{ GHz})] \approx 2.3$. This agrees with the local FIR/radio correlation and supports the idea that the same population of galaxies accounts for the star-forming radio and FIR backgrounds.

The Herschel PACS Evolutionary Probe (PEP) resolved $74 \pm 5\%$ of the $\lambda = 160 \mu\text{m}$ background into individually detected galaxies stronger than about 3 mJy, and Berta et al. (2011) used a $P(D)$ analysis to raise the resolved fraction to $\sim 89\%$ above ~ 0.3 mJy. The sensitivity limits of the VLA ($\theta = 8''$ FWHM resolution) and Herschel PEP $\lambda = 160 \mu\text{m}$ ($\theta \approx 11''$ FWHM resolution) $P(D)$ distributions to galaxies obeying the FIR/radio

correlation are about equal, and the same fraction of the star-forming galaxy background has been resolved at radio and FIR wavelengths. Converting the direct and $P(D)$ counts at $\lambda = 160 \mu\text{m}$ to 1.4 GHz using the relation $\log[S(160 \mu\text{m})/S(1.4 \text{ GHz})] = 2.5$ allows them to be compared directly with the Condon (1984b) 1.4 GHz count model for star-forming galaxies (dotted curve in Fig. 14); the agreement is well within the statistical errors.

6. THE ARCADE2 EXTRAGALACTIC BACKGROUND AND CONSTRAINTS ON NEW POPULATIONS OF RADIO SOURCES

If the extragalactic source background is really $T_b \sim 100$ mK at 1.4 GHz and 13 mK at 3.02 GHz, then it has been resolved into the known source populations powered by AGNs and star formation. However, all of the faint-source counts are based on interferometric images which are insensitive to a smooth background, the 2.7 K CMB for example. We cannot rule out a sufficiently smooth distribution of faint radio sources that contributes significantly to the extragalactic background brightness, but we can set strong lower limits to the numbers of sources needed to make the background smooth enough to agree with our narrow 3.02 GHz $P(D)$ distribution.

The ARCADE2 measurement of the extragalactic sky temperature in the 3–90 GHz frequency range (Fixsen et al. 2011) recently reported a surprising extragalactic excess over the CMB. Its brightness spectrum is

$$\left(\frac{T_b}{\text{K}}\right) = (24.1 \pm 2.1) \left(\frac{\nu}{0.31 \text{ GHz}}\right)^{-2.599 \pm 0.036} \quad (29)$$

between 22 MHz to 10 GHz. This is $T_b = 480 \pm 50$ mK at $\nu = 1.4$ GHz and $T_b = 65 \pm 8$ mK at $\nu = 3.02$ GHz, much higher than the 100 ± 10 mK and 13 ± 1.3 mK attributable to known extragalactic radio sources at 1.4 GHz and 3.02 GHz, respectively.

One possible explanation is the existence of a new population of faint extragalactic sources that contributes $\Delta T_b \approx 480 - 100 = 380 \pm 50$ mK at 1.4 GHz and $\Delta T_b \approx 65 - 13 = 52 \pm 8$ mK at 3.02 GHz to the sky background. A truly diffuse synchrotron background produced by relativistic electrons in intergalactic space far from individual galaxies was ruled out by Singal et al. (2010) on the grounds that inverse-Compton scattering of those electrons radiating in weak ($B < 1 \mu\text{G}$) intergalactic magnetic fields would exceed the observed X-ray and γ -ray backgrounds. Singal et al. (2010) also pointed out that the diffuse emission from clusters of galaxies has a spectrum that is too steep ($\alpha < -1$) to explain the ARCADE2 excess, as does emission from shocks in the cosmic web (Brown 2011).

Equation 3 constrains the source count of any new population of faint unresolved sources contributing ΔT_b to the sky brightness. Figure 15 plots $\log[S^2n(S)]$ as a function of $\log(S)$ for the known populations of radio sources powered by AGN and by star-forming galaxies; they appear as two broad peaks centered near $\log(S_{\text{pk}}) \sim -1$ and $\log(S_{\text{pk}}) \sim -5$, respectively. The regions near these peaks contribute most to the sky brightness, and each peak is well represented by the parabolic Taylor-series approximation $\log[S^2n(S)] \approx a - b[\log(S) - \log(S_{\text{pk}})]^2$ or

$$S^2n(S) \approx A \exp\left\{-4 \ln(2) \frac{[\log(S) - \log(S_{\text{pk}})]^2}{\phi^2}\right\}, \quad (30)$$

where ϕ is the logarithmic FWHM of the Gaussian and S_{pk} is the flux density of the peak. The peak amplitude A (the peak brightness in units of Jy sr^{-1}) required for a new population characterized by a Gaussian of FWHM ϕ to add ΔT_{b} to the background can be found by inserting equation 30 into equation 3 and integrating over all flux densities ($S_0 = 0$); it is

$$A\phi = \frac{4k_{\text{B}}\nu^2}{\ln(10)c^2} \left[\frac{\ln(2)}{\pi} \right]^{1/2} \Delta T_{\text{b}}. \quad (31)$$

A and ϕ are individually free, but their product $A\phi$ is fixed by ΔT_{b} .

Figure 15 shows three examples of source counts, each of which yield $\Delta T_{\text{b}} \approx 380$ mK at $\nu = 1.4$ GHz. The dotted, dashed, and continuous curves correspond to logarithmic FWHMs $\phi = 0.2, 1.0,$ and 2.0 in equation 30, and their peak amplitudes calculated from equation 31 are $\log[A(\text{Jy sr}^{-1})] \approx 4.67, 3.97,$ and 3.67 , respectively. The value of ΔT_{b} is independent of S_{pk} , so these parabolic curves are free to shift horizontally when constrained by sky brightness alone. However, a large value of S_{pk} decreases the number of sources per square arcmin needed to produce the excess background and increases the Poisson fluctuations in sky brightness, so the width of our observed $P(D)$ distribution sets upper limits to the values of S_{pk} associated with these three examples. If the background is too bright and smooth, the number of faint radio sources required will exceed the total number of galaxies.

The narrowest possible peak ($\phi \ll 1$) needs the smallest number N of sources per beam solid angle to produce a given T_{b} . In that unrealistic limit, all of the new sources have nearly the same very low flux density S_{pk} and their noiseless $P(D)$ distribution is nearly Gaussian. To set a very conservative upper limit to the rms width of this Gaussian, we found the widest Gaussian consistent with our observed $P(D)$ distribution. It is shown in Figure 16, and its rms is $\sigma \approx 0.70 \mu\text{Jy beam}^{-1} \approx 1.47$ mK at $\nu = 3.02$ GHz. To avoid excessive Poisson noise, the minimum number N of sources per beam solid angle $\Omega_{\text{b}} \approx 0.020$ arcmin² must be

$$N > \left(\frac{\Delta T_{\text{b}}}{\sigma} \right)^2 = \left(\frac{52 \text{ mK}}{1.47 \text{ mK}} \right)^2 \approx 1.3 \times 10^3, \quad (32)$$

implying $> 6 \times 10^4$ radio sources per arcmin², and the maximum source flux density consistent with the background brightness is $S_{\text{pk}} < 34$ nJy at 1.4 GHz if $\alpha = -0.7$. This is slightly below the hoped-for $5\sigma_{\text{n}} = 45$ nJy sensitivity limit of the full 12000 m² K⁻¹ SKA after 1 megasecond of integration, so even if such faint sources exist, it will be a long time before they can be detected individually.

Broader flux distributions can only raise the minimum source density and lower the peak flux density. If $\phi = 1$ ($\phi = 2$), then there must be more than 1.6×10^5 (3×10^6) sources per arcmin² with peaks at $S_{\text{pk}} < 22$ nJy (< 5 nJy). The dotted, dashed, and continuous curves in Figure 15 are as far right as allowed by the $P(D)$ smoothness constraint. They could be shifted to the left, but that would only increase the implied sky density of radio sources. Our new constraint on the smoothness of the background forces the ‘‘bump’’ in the weighted source

count at μJy levels proposed by Seiffert et al. (2011) and Vernstrom & Wall (2011) to much lower flux levels.

There are only 10^4 galaxies brighter than $m_{\text{AB}} = +29$ in the 11 arcmin² Hubble Ultra Deep Field (HUDF) (Beckwith et al. 2006), or $\approx 10^3$ galaxies per arcmin², about two orders magnitude lower than the minimum sky density of faint radio sources needed to produce the smooth ARCADE2 excess background. The HUDF can detect galaxies 2 mag fainter than L^* out to redshifts $z \approx 6$, so it appears that the smooth ARCADE2 background cannot be produced by galaxies or by objects located in or near individual galaxies (e.g., multiple radio supernovae or gamma-ray bursts in galaxies, radio-quiet quasars, radio halos smaller than 8 arcsec in diameter) or by star-forming galaxies that are more radio-loud than expected from the FIR/radio correlation (Singal et al. 2010). Might faint sources produced by WIMP annihilations or decays in dark-matter (DM) halos (Fornengo et al. 2011) be sufficiently numerous to produce a sufficiently smooth background? Annihilation in DM halos around galaxies would violate our smoothness constraint, leaving only the possibility of preferential DM annihilation in high-redshift mini-halos. If our 3.02 GHz $P(D)$ smoothness constraint and the Fixsen et al. (2011) 3.3 GHz excess brightness are both correct, then a very numerous ($N > 10^{13}$ over the whole sky) and unexpected population of radio sources not associated with galaxies has been discovered.

7. SUMMARY

We used 21 antennas in the Karl G. Jansky VLA to observe a single field at S band (2–4 GHz) with a FWHM resolution $\theta = 8''$ and reached an rms noise $\sigma_{\text{n}} \approx 1 \mu\text{Jy beam}^{-1}$ near the image center after 50 hours of integration time. The image is confusion limited with an ‘‘rms’’ confusion level $\sigma_{\text{c}}^* \approx 1.2 \mu\text{Jy beam}^{-1}$ at $\nu = 3.02$ GHz.

The 3.02 GHz differential source count was derived from the confusion $P(D)$ distribution. For comparison with published source counts, we converted it to 1.4 GHz via the effective spectral index $\langle \alpha \rangle \approx -0.7$. The power-law approximation $n(S) \propto S^{-\gamma}$ to the 1.4 GHz source count has a slope approaching $\gamma \approx 1.5$ near $1 \mu\text{Jy}$, significantly lower than the slopes of published counts above $10 \mu\text{Jy}$. If the faintest radio sources have median angular size $\langle \theta_{\text{s}} \rangle \leq 1''$ as expected for emission coextensive with star-forming regions in distant galaxies, the natural confusion limit for source detection is not more than $5\sigma_{\text{c}}^* \approx 0.01 \mu\text{Jy}$ at 1.4 GHz, and the continuum sensitivity of the planned SKA will not be limited by natural confusion. The observed count is well fit by evolutionary models in which the local radio luminosity functions of all sources associated with both AGNs and star formation evolve at the same rate. This is broadly consistent with the correlation of black hole and stellar bulge masses in massive elliptical galaxies, although this correlation is not yet well established for the lower-mass black holes and bulges in late-type galaxies (Greene et al. 2010).

The brightness-weighted count $S^2 n(S)$ is clearly converging below $10 \mu\text{Jy}$. Our image has resolved about 96% of the radio background produced by all galaxies ($T_{\text{b}} \approx 100$ mK at 1.4 GHz and $T_{\text{b}} \approx 13$ mK at 3 GHz). Nearly 100% of the ≈ 63 mK AGN-powered

background at 1.4 GHz has been resolved. The remaining ≈ 37 mK comes from star-forming galaxies that obey the FIR/radio correlation and account for most of the extragalactic background at $\lambda = 160 \mu\text{m}$. We resolved about 89% of the star-forming galaxy contribution.

The ARCADE2 balloon experiment indicated a non-thermal excess brightness over the Galaxy, the CMB, and that expected from known populations of radio sources in

galaxies. At 3.02 GHz this excess brightness temperature is 52 ± 8 mK. Our narrow 3.02 GHz $P(D)$ distribution implies that the excess background must be very smooth. Any new discrete-source population able to produce such a bright and smooth background is far too numerous to be associated with galaxies brighter than $m_{\text{AB}} = +29$.

Facilities: VLA

APPENDIX

NOISE DISTRIBUTIONS IN SYNTHESIS IMAGES

In the noise-limited outer regions of our image, the pixels have a Gaussian brightness distribution with rms $\sigma_n \approx 1 \mu\text{Jy beam}^{-1}$. What is the rms fractional uncertainty ($\Delta\sigma_n/\sigma_n$) of the rms noise averaged over a large solid angle $\Omega \gg \Omega_b$? The answer is complicated because the pixel values are not independent. Just as the limited (u, v) plane coverage of data going into our image acts as a convolving filter to smooth our image of the sky brightness distribution, it acts as a filter to smooth the image noise distribution. The smoothing function for both sky brightness and noise is the synthesized beam. Our synthesized beam is closely approximated by a circular Gaussian (Fig. 2) with FWHM $\theta_s = 8$ arcsec, so its normalized (peak gain $G = 1$) gain profile can be written

$$G(\theta, \phi) = \exp\left[-4 \ln 2 \left(\frac{\theta}{\theta_s}\right)^2\right]. \quad (\text{A1})$$

The corresponding synthesized beam solid angle is

$$\Omega_b \equiv \int G d\Omega = \frac{\pi\theta_s^2}{4 \ln 2} \approx 1.13\theta_s^2. \quad (\text{A2})$$

It is easy to calculate ($\Delta\sigma_n/\sigma_n$) for a square top-hat beam with FWHM W :

$$G(x, y) = 1, \quad -W/2 < x < +W/2, \quad -W/2 < y < +W/2 \quad (\text{A3})$$

and $G(x, y) = 0$ elsewhere, so the beam solid angle is $\Omega_b = W^2$. A large area Ω can be tiled by $N = \Omega/\Omega_b \gg 1$ nonoverlapping beam solid angles. Averaging their N independent noise values divides the rms noise by $N^{1/2}$, so

$$\frac{\Delta\sigma_n}{\sigma_n} = \left(\frac{\Omega_b}{\Omega}\right)^{1/2} = \left(\frac{1}{N}\right)^{1/2} \quad (\text{A4})$$

in this case. This sort of argument seems to underly the common but incorrect belief that equation A4 is true for all beamshapes.

The problem is that noise variance σ_n^2 , rather than noise rms σ_n , adds under convolution. The amount of noise smoothing is proportional to the ‘‘noise beam solid angle’’

$$\Omega_n \equiv \int G^2 d\Omega \quad (\text{A5})$$

rather than to the beam solid angle given by equation A2. Only in the case of a top-hat beam does $\Omega_n = \Omega_b$. The square of a Gaussian is also a Gaussian, but its FWHM is $\theta_s/2^{1/2}$ so $\Omega_n = \Omega_b/2$ for a Gaussian beam. Thus

$$\frac{\Delta\sigma_n}{\sigma_n} = \left(\frac{\Omega_n}{\Omega}\right)^{1/2} = \left(\frac{1}{2N}\right)^{1/2}. \quad (\text{A6})$$

To convince skeptics that this result correctly describes our data, we selected 31 independent source-free regions from our image, uncorrected for primary attenuation so $\sigma_n \approx 1 \mu\text{Jy beam}^{-1}$ in all regions. Each region covers $100 \times 100 = 10^4$ pixels $\approx 1''252$ on a side, so $\Omega_b \approx 46.3$ pixels and there are $N \approx 216 \gg 1$ beam solid angles per region. If equation A4 were correct for our Gaussian synthesized beam, we would expect

$$\frac{\Delta\sigma_n}{\sigma_n} \approx 0.068. \quad (\text{A7})$$

Equation A6 predicts the lower value

$$\frac{\Delta\sigma_n}{\sigma_n} \approx 0.048. \quad (\text{A8})$$

In the 31 regions the observed mean and its rms scatter are

$$\frac{\Delta\sigma_n}{\sigma_n} = 0.040 \pm 0.007. \quad (\text{A9})$$

This is consistent with equation A6 but is four standard deviations below equation A4.

A similar argument applies to calculations of survey speed. How much time is needed to make a survey covering a large solid angle $\Omega = N\Omega_b$ using a single Gaussian beam? If staring time τ is needed to reach the desired survey sensitivity at the center of one beam, the time needed to make the whole survey is $t \approx 2N\tau$, twice the frequently quoted $t \approx N\tau$ (Condon et al. 1998).

Finally, the effective beam area Ω_e for confusion (Eq. 18) becomes $\Omega_e = \int G^2 d\Omega = \Omega_n$ when $\gamma \rightarrow 3$. In this limit, the confusion fluctuations are dominated by the very faintest sources and the $P(D)$ distribution becomes a Gaussian, just like a noise distribution.

REFERENCES

- Auriemma, C., Perola, G. C., Ekers, R. et al. 1977, A&A, 57 41
 Beckwith, S. V. W. et al. 2006, AJ, 132, 1729
 Berkhuijsen, E. M. 1984, A&A, 140, 431
 Berta, S. et al. 2011, A&A, 532, A49
 Bolton, J. S., Gardner, F. F., & Mackay, M. B. 1964, AuJP, 17, 340
 Bondi, H., & Gold, T. 1948, MNRAS, 108, 252
 Boyle, B. J., & Terlevich, R. J. 1998, MNRAS, 293, L39
 Briggs, D. S. 1995, AAS, 187, 112.02
 Brown, S. 2011, JApA., 32, 577
 Condon, J. J. 1974, ApJ, 188, 279
 Condon, J. J. 1984, ApJ, 284, 44
 Condon, J. J. 1984, ApJ, 287, 461
 Condon, J. J. 1989, ApJ, 338, 13
 Condon, J. J. 1992, ARA&A, 30, 575
 Condon, J. J. 1997, PASP, 109, 166
 Condon, J. J. 2007, in ASP Conf. Ser. 380, At the Edge of the Universe: Latest Results from the Deepest Astronomical Surveys, ed. J. Afonso, H. C. Ferguson, B. Mobasher, & R. Norris, p. 189
 Condon, J. J. 2009, SKA Memo 114 <http://www.skatelescope.org/publications/>
 Condon, J. J., Cotton, W. D., & Broderick, J. J. 2002, AJ, 124, 675
 Condon, J. J., Cotton, W. D., Greisen, E. W. et al. 1998, AJ, 115, 1693
 Condon, J. J., & Mitchell, K. J. 1984, AJ, 89, 610
 Cotton, W. D. 2008, PASP, 120, 439
 De Zotti, G., Masardi, M., Negrello, M., & Wall, J. V. 2010, A&AR, 18, 1
 Fixsen, D. J., Dwek, E., Mather, J. C., Bennett, C. L., & Shafer, R. A. 1998, ApJ, 508, 123
 Fixsen, D. J., Kogut, A., Levin, S. M. et al. 2011, ApJ, 734:5
 Fornengo, N., Lineros, R., Regis, M., & Taoso, M. 2011, PRL, 107, 271302
 Glenn, J., Conley, A., Béthermin, M. et al. 2010, MNRAS, 409, 109
 Gower, J. F. R. 1966, MNRAS, 133, 151
 Greene, J. E., Peng, C. Y., Kim, M. et al. 2010, ApJ, 721, 26
 Hewish, A. 1961, MNRAS, 123, 167
 Hopkins, A. 2007, in ASP Conf. Ser. 380, At the Edge of the Universe: Latest Results from the Deepest Astronomical Surveys, ed. J. Afonso, H. C. Ferguson, B. Mobasher, & R. Norris, p. 423
 Hoyle, F. 1948, MNRAS, 108, 372
 Hughes, A., Staveland-Smith, L., Kim, S., Wolleben, M., & Filipovic, M. 2007, MNRAS, 382, 543
 Hummel, E. 1980, A&AS, 41, 151
 Ivison, R. J., Magnelli, B., Ibar, E. et al. 2010, A&A, 518, L31
 Kellermann, K. I., Pauliny-Toth, I. I. K., & Williams, P. J. S. 1969, ApJ, 157, 1
 Lagache, G., Abergel, A., Boulanger, F., Désert, F. X., & Puget, J.-L. 1999, A&A, 344, 322
 Longair, M. S. 1966, MNRAS, 133, 421
 Lonsdale, C. J., Smith, H. E., Rowan-Robinson, M. et al. 2003, PASP, 115 897
 Magorrian, J., Tremaine, S., Richstone, D. et al. 1998, AJ, 115, 2285
 Mauch, T., & Sadler, E. M. 2007, MNRAS, 375, 931
 Massardi, M., Bonaldi, A., Negrello, M. et al. 2010, MNRAS, 404, 532
 Mills, B., & Slee, O. B. 1957, AuJP, 10, 162
 Mitchell, K. J., & Condon, J. J. 1985, AJ, 90, 1957
 Murdoch, H. S., Crawford, D. F., & Jauncey, D. L. 1973, ApJ, 183, 1
 Norris, R. P. et al. 2011, PASA, 28, 215
 Owen, F. N., & Morrison, G. E. 2008, AJ, 136, 1889
 Ryle, M. 1955, Observatory, 75, 137
 Ryle, M., & Neville, A. C. 1962, MNRAS, 125, 39
 Ryle, M., & Scheuer, P. A. G. 1955, PRSPSA, 230, 448
 Scheuer, P. A. G. 1957, Proc. Cambridge Phil. Soc., 53, 764
 Seiffert, M., Fixsen, D. J., Kogut, A. et al. 2011, ApJ, 734:6
 Singal, J., Stawarz, L., Lawrence, A., & Petrosian, V. 2010, MNRAS, 409, 1172
 Vernstrom, T., Scott, D., & Wall, J. V. 2011, MNRAS, 415, 3641
 Wall, J. V. 1997 in Astrophysics and Space Science Library (ASSL) Series 226, Observational Cosmology with the New Radio Surveys, ed. M. N. Bremer, N. Jackson, & I. Perez-Fournon, p. 129
 Wilman, R. J., Miller, L., Jarvis, M. J. et al. 2008, MNRAS, 388, 1335
 Windhorst, R. A., Fomalont, E. B., Partridge, R. B., & Lowenthal, J. D. 1993, ApJ, 405, 498
 Windhorst, R. A., Miley, G. K., Owen, F. N., Kron, R. G., & Koo, D. C. 1985, ApJ, 289, 494

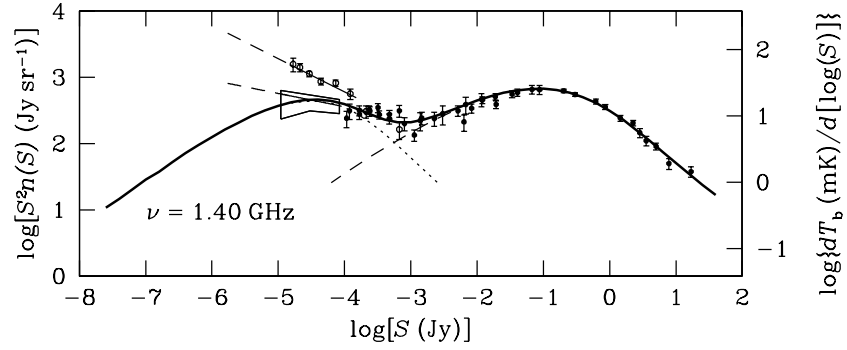


Figure 1. Published 1.4 GHz source counts. The brightness-weighted source count $S^2n(S)$ is proportional to the contribution per decade of flux density to the sky background temperature T_b . The filled points at $\log[S \text{ (Jy)}] > -3$ are from Condon (1984a) and Mitchell & Condon (1985). The polygon encloses the range of 1.4 GHz counts consistent with confusion (Mitchell & Condon 1985), and the straight line inside the box is the best power-law fit to the confusion data. The open data points and their power-law fit (upper straight line) indicate the Owen & Morrison (2008) source count. The solid curve is the Condon (1984b) model count composed of sources powered primarily by AGNs (dashed curve) and by star formation (dotted curve). Left ordinate: log of the 1.4 GHz source count $S^2n(S)$ (Jy sr^{-1}). Right ordinate: log of the source contribution $dT_b/d[\log(S)]$ (mK) to the 1.4 GHz background per decade of flux density.

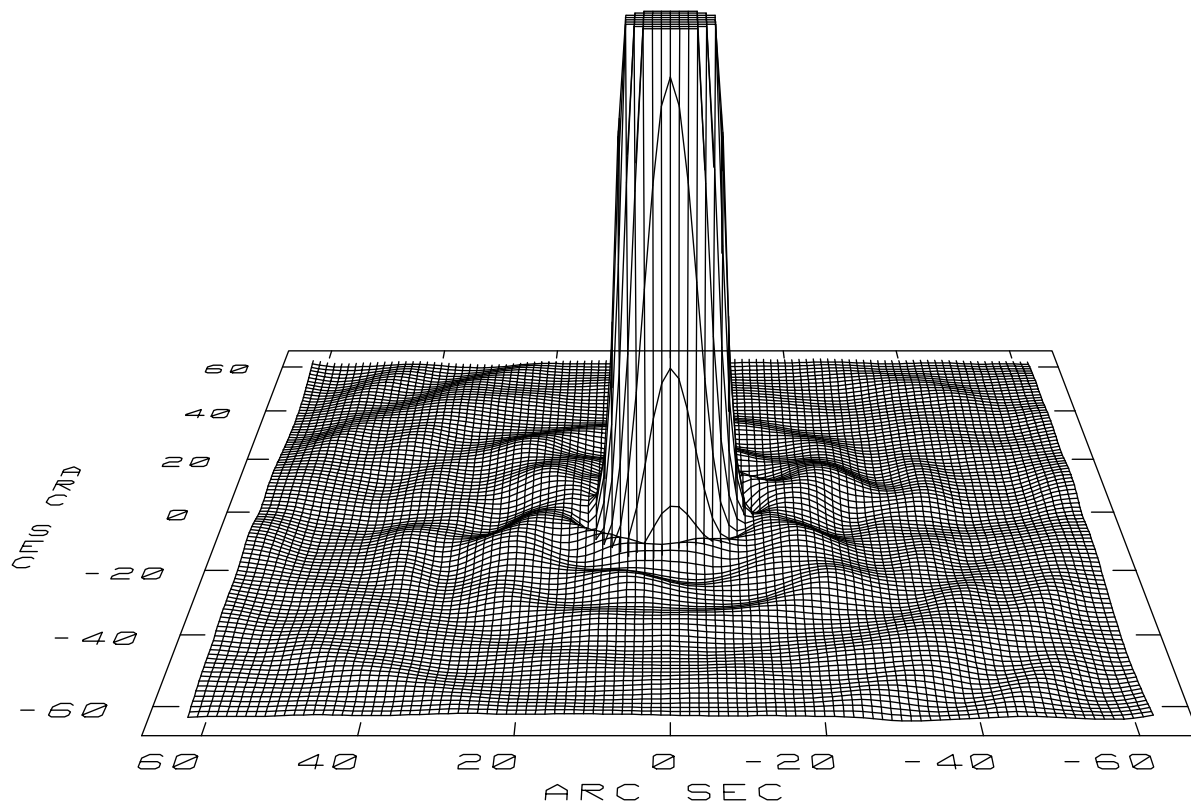


Figure 2. Dirty-beam profile. The dirty beam in our wideband image, shown truncated at 20% of its peak to demonstrate that the highest sidelobe level is under 1%.

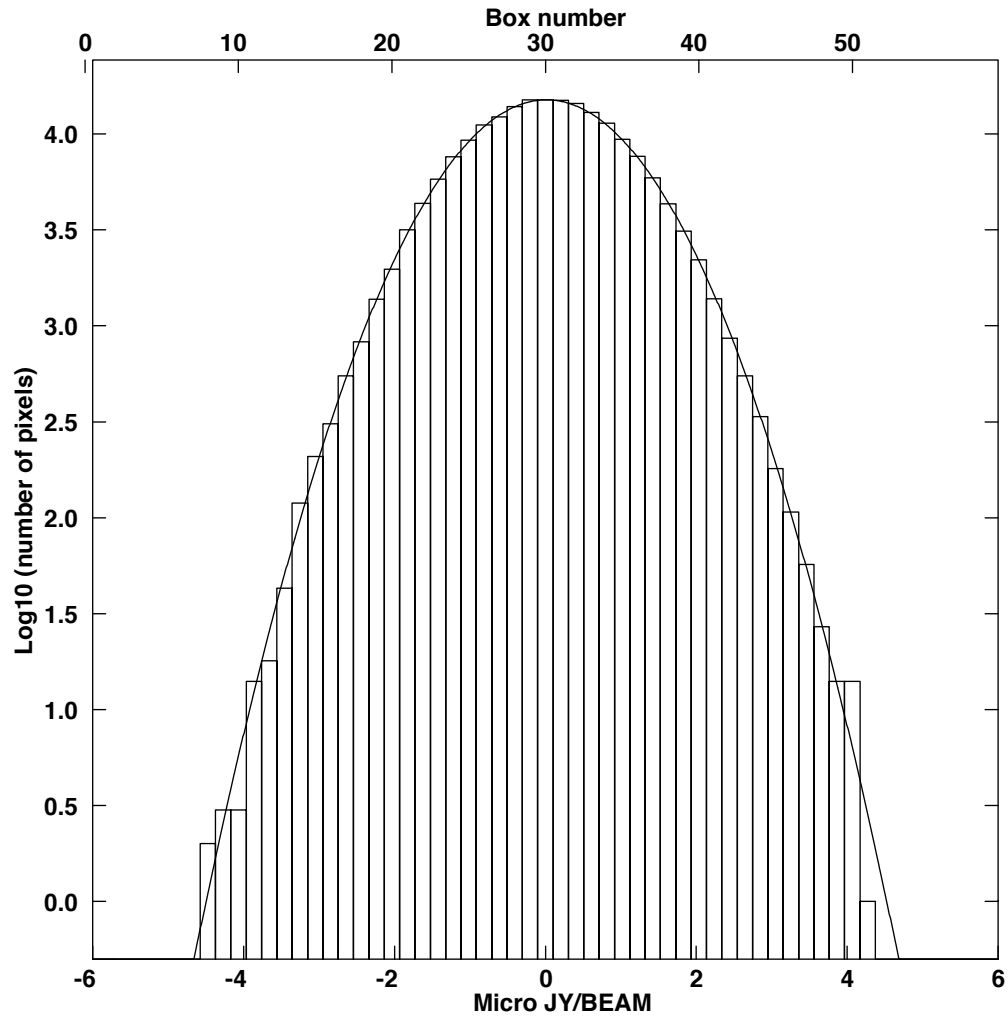


Figure 3. Noise distribution. This noise distribution from one source-free region near the edge of our wideband image is a nearly perfect Gaussian with rms $\sigma = 1.02 \mu\text{Jy beam}^{-1}$; it appears as a parabola on this logarithmic plot. Abscissa: Log of the number of pixels per bin of width $0.2 \mu\text{Jy beam}^{-1}$. Ordinate: Peak flux density ($\mu\text{Jy/beam}$).

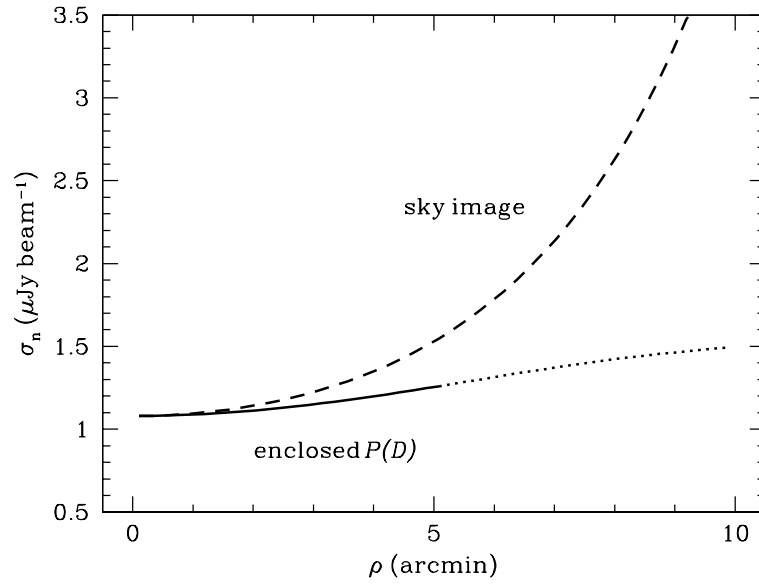


Figure 4. Noise levels in the final image. The rms noise σ_n in the ring of radius ρ in the sky image (dashed curve) and in the weighted $P(D)$ distribution of points inside the circle of radius ρ . Abscissa: Offset from the pointing center (arcmin). Ordinate: Root-mean-square noise ($\mu\text{Jy beam}^{-1}$).

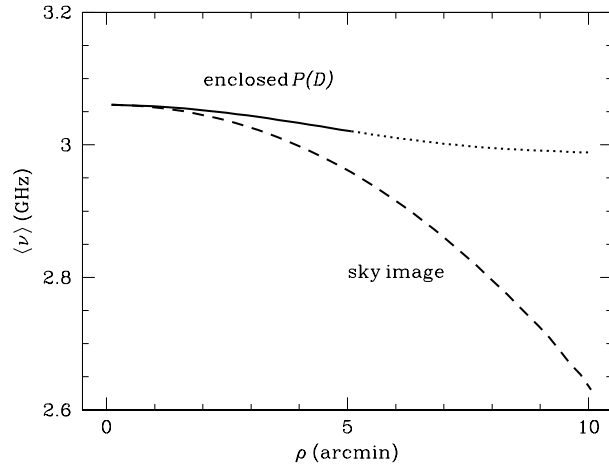


Figure 5. Effective frequencies in the final image. The effective frequency $\langle \nu \rangle$ is the frequency at which the flux density of a source with spectral index $\alpha = -0.7$ equals the local flux density in the ring of radius ρ in the sky image (dashed curve) or the average flux density of the weighted $P(D)$ distribution of points inside the circle of radius ρ . Abscissa: Offset from the pointing center (arcmin). Ordinate: Effective frequency (GHz).

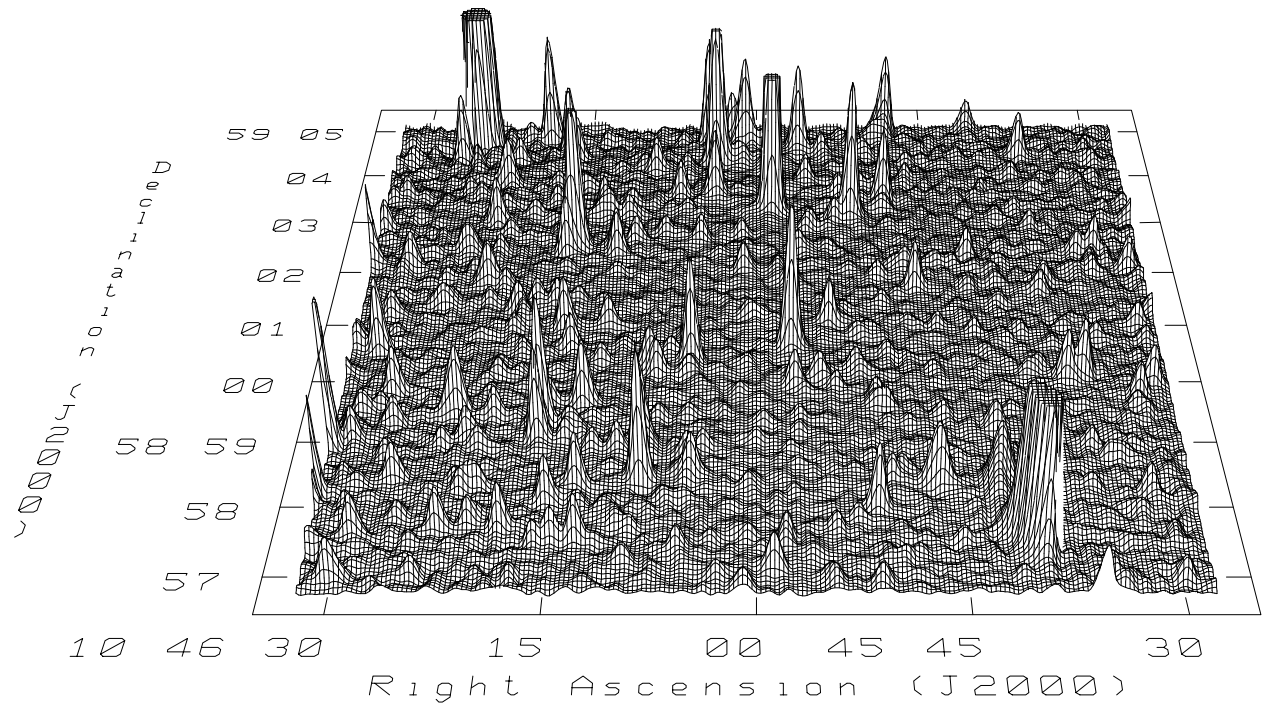


Figure 6. Confusion profile. This profile plot shows the 3 GHz confusion amplitude in an 8 arcsec FWHM beam, truncated at 100 microJy/beam.

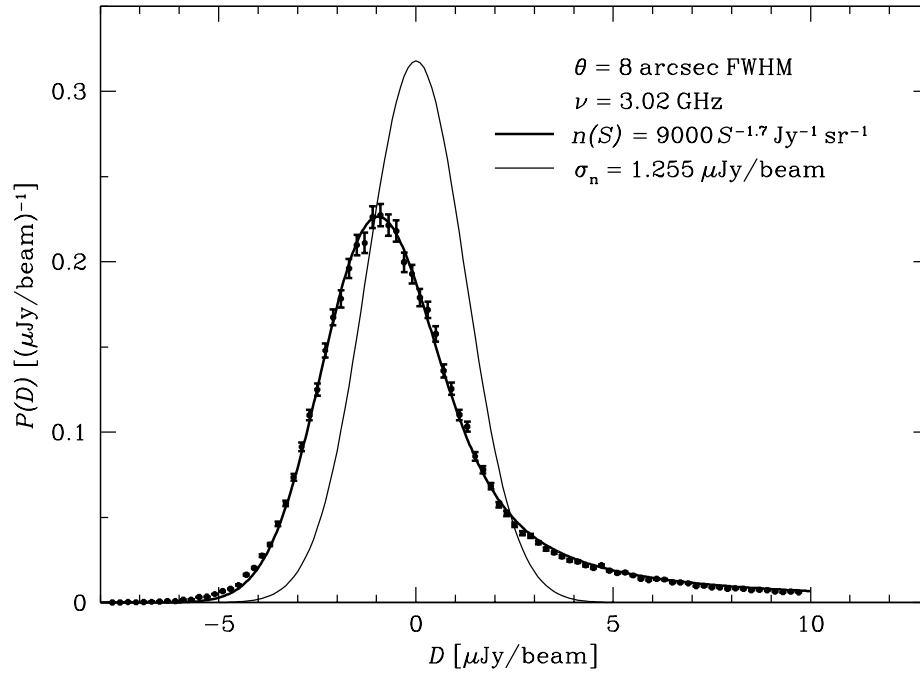


Figure 7. Observed $P(D)$ distribution. The observed probability distribution $P(D)$ (data points with error bars) of “deflections” or peak flux densities at 3.02 GHz within a circle of radius $\rho = 5$ arcmin. The PSF is a circular Gaussian with FWHM $\theta = 8''$. The noise has a Gaussian amplitude distribution with rms $\sigma_n = 1.255 \mu\text{Jy}/\text{beam}$ (thin curve). The thick fitted curve is the convolution of the noise distribution with the noise-free $P(D)$ distribution (Condon 1974) of the power-law source distribution $n(S) = 9000 S^{-1.7} \text{ Jy}^{-1} \text{ sr}^{-1}$. Abscissa: Deflection or peak flux density ($\mu\text{Jy}/\text{beam}$) at 3.02 GHz. Ordinate: Probability density ($\mu\text{Jy beam}^{-1}$).

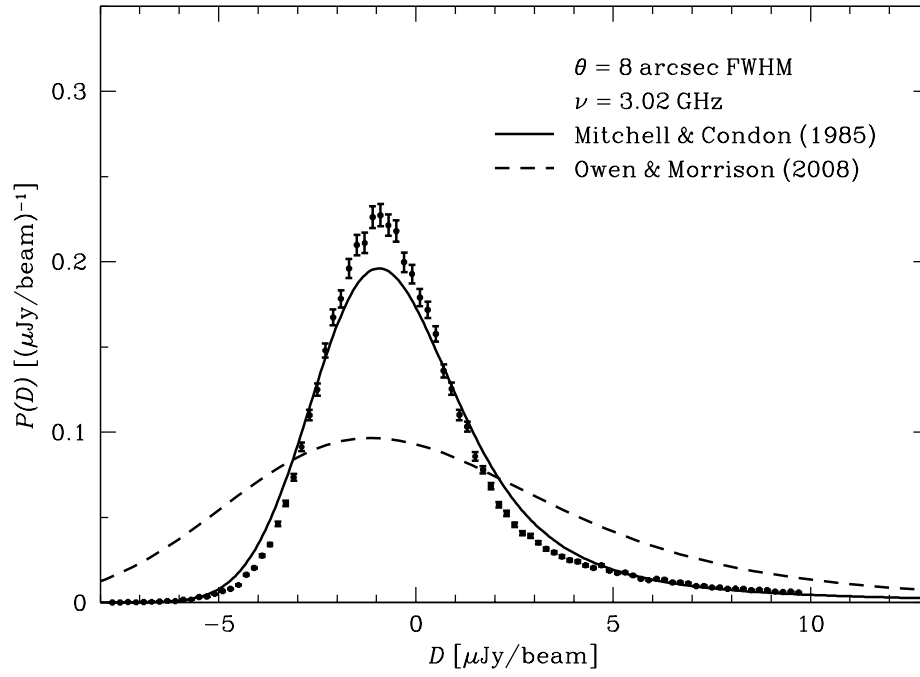


Figure 8. Expected $P(D)$ distributions from extrapolations of published counts. This figure compares the observed $P(D)$ distribution (data points with error bars) at 3.02 GHz with power-law extrapolations of deep source counts measured at 1.4 GHz, assuming a mean spectral index $\langle\alpha\rangle = -0.7$. The continuous curve indicates the expected 3.02 GHz $P(D)$ distribution from the power-law extrapolation of the Mitchell & Condon (1985) 1.4 GHz source count $n(S) = 57S^{-2.2} \text{ Jy}^{-1} \text{ sr}^{-1}$, and the dashed curve corresponds to the Owen & Morrison (2008) 1.4 GHz source count $n(S) = 6S^{-2.5} \text{ Jy}^{-1} \text{ sr}^{-1}$. Abscissa: Deflection or peak flux density ($\mu\text{Jy}/\text{beam}$) at 3.02 GHz. Ordinate: Probability density ($\mu\text{Jy beam}^{-1}$).

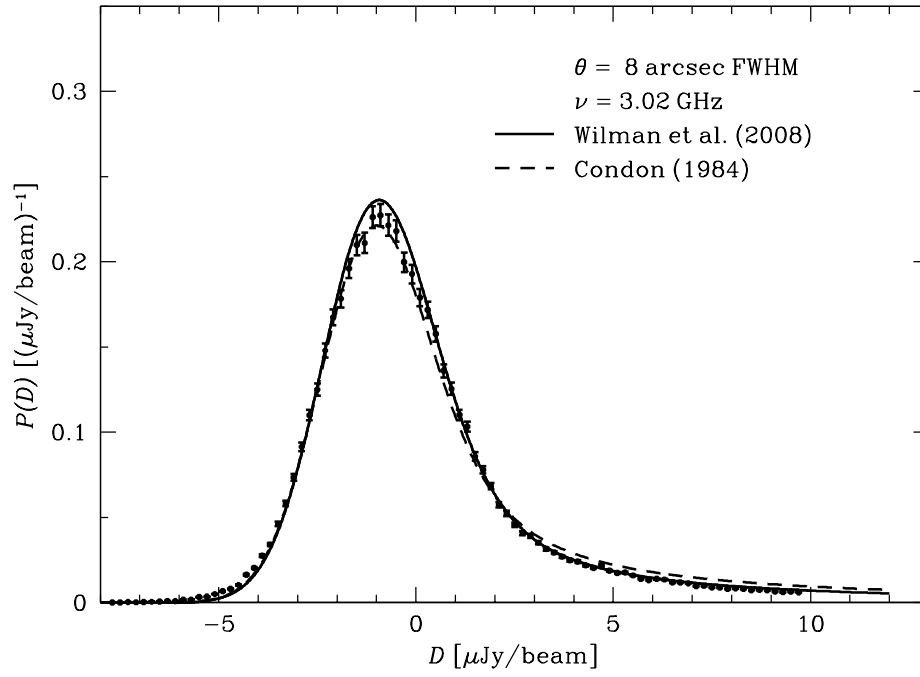


Figure 9. Expected $P(D)$ distributions from source-count models. This figure compares the observed $P(D)$ (data points with error bars) at 3.02 GHz with power-law fits to model source counts at 1.4 GHz, assuming a mean spectral index $\langle\alpha\rangle = -0.7$. The continuous curve indicates the expected 3.02 GHz $P(D)$ distribution for the 1.4 GHz source count $n(S) = 3.45 \times 10^4 S^{-1.6}$ predicted by Wilman et al. (2008) and the dashed curve corresponds to $n(S) = 1.2 \times 10^5 S^{-1.5}$ predicted by Condon (1984b). Abscissa: Deflection or peak flux density ($\mu\text{Jy}/\text{beam}$) at 3.02 GHz. Ordinate: Probability density ($\mu\text{Jy beam}^{-1}$).

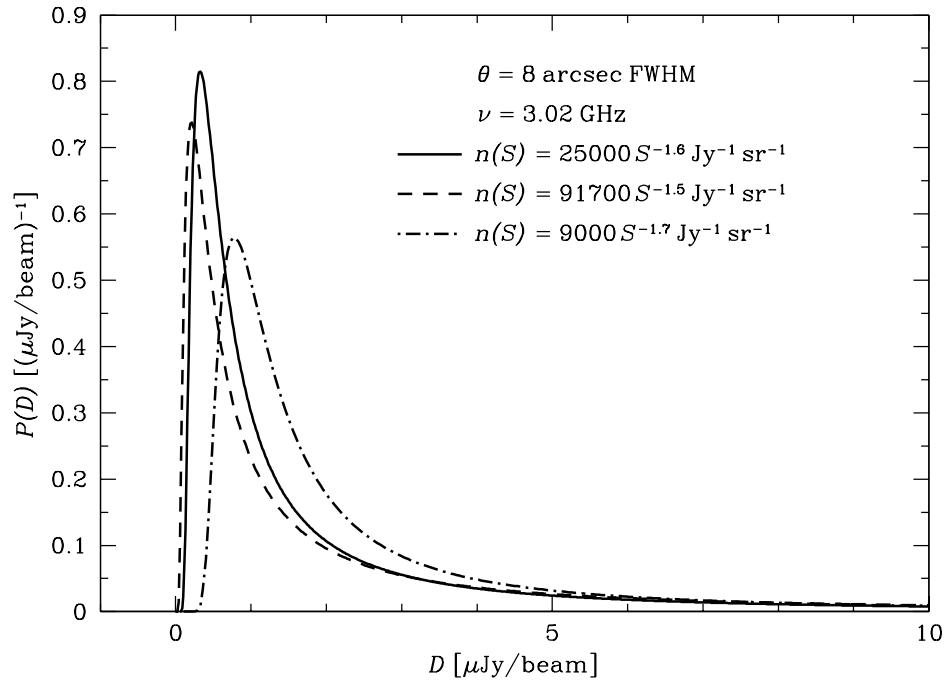


Figure 10. Noise-free $P(D)$ distributions. The range of noise-free 3.02 GHz $P(D)$ distributions in a $FWHM = 8''$ Gaussian beam calculated for three power-law approximations to the 3.02 GHz source count that are consistent with our data: $n(S) = 25000 S^{-1.6} \text{ Jy}^{-1} \text{ sr}^{-1}$ (Wilman et al. 2008), $n(S) = 91700 S^{-1.5} \text{ Jy}^{-1} \text{ sr}^{-1}$ (Condon 1984b), and $n(S) = 9000 S^{-1.7} \text{ Jy}^{-1} \text{ sr}^{-1}$ (this paper). Abscissa: Deflection or peak flux density ($\mu\text{Jy}/\text{beam}$) at 3.02 GHz. Ordinate: Probability density ($\mu\text{Jy beam}^{-1}$).

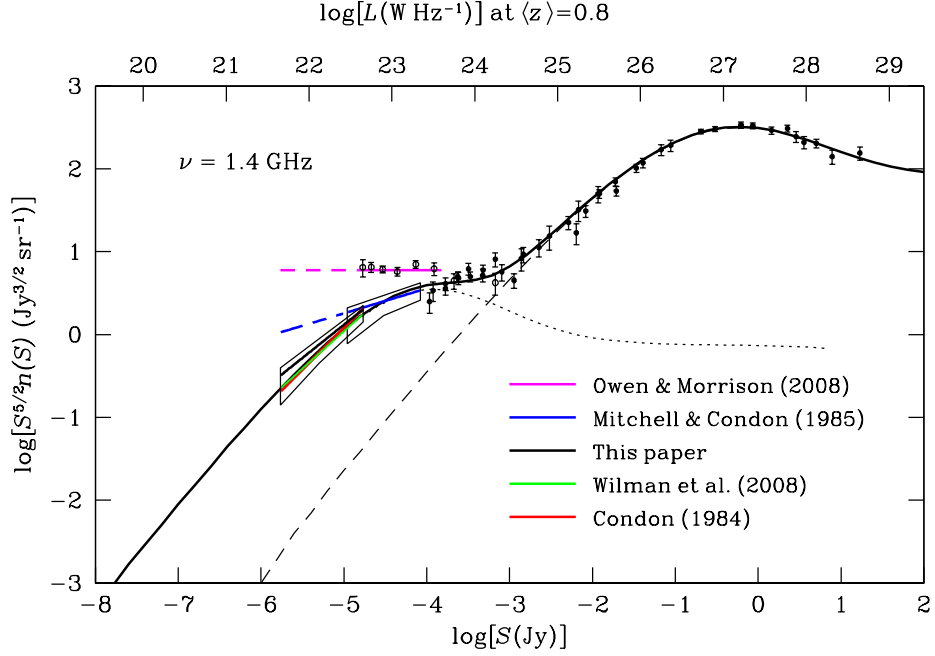


Figure 11. Euclidean-normalized source counts. The plotted source counts at 1.40 GHz are based on individual sources (data points), the 1.4 GHz $P(D)$ distribution (blue line and surrounding error box) from Mitchell & Condon (1985), and our 3.02 GHz $P(D)$ distribution (black line and surrounding error box) converted to 1.40 GHz via a mean spectral index $\alpha = -0.7$. The red and green lines are power-law approximations to the 1.40 GHz models of Condon (1984b) and Wilman et al. (2008), respectively. The dashed curve is the contribution of AGNs and the dotted curve is the contribution of star-forming galaxies, from the Condon (1984b) model. Lower abscissa: log flux density (Jy) at 1.40 GHz. Upper abscissa: log spectral luminosity (W Hz^{-1}) at 1.4 GHz in the source frame for sources at the typical redshift $\langle z \rangle \approx 0.8$. Ordinate: Source count normalized by the source count $n(S) \propto S^{-5/2}$ in a static Euclidean universe ($\text{Jy}^{3/2} \text{sr}^{-1}$).

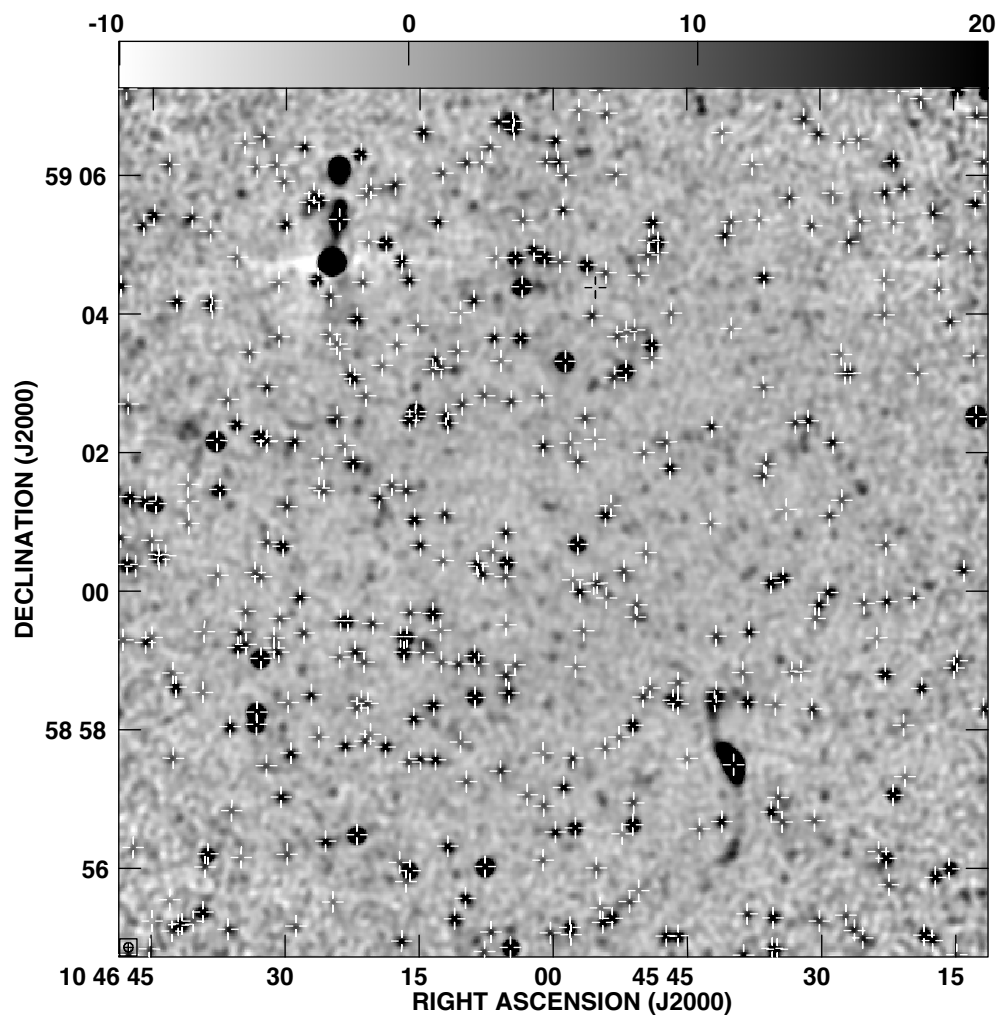


Figure 12. Gray-scale sky image at 3 GHz. Sources in the Owen & Morrison (2008) catalog are indicated by crosses on our gray-scale image. The wedge indicates 3 GHz brightnesses between -10 and $+20 \mu\text{Jy beam}^{-1}$.

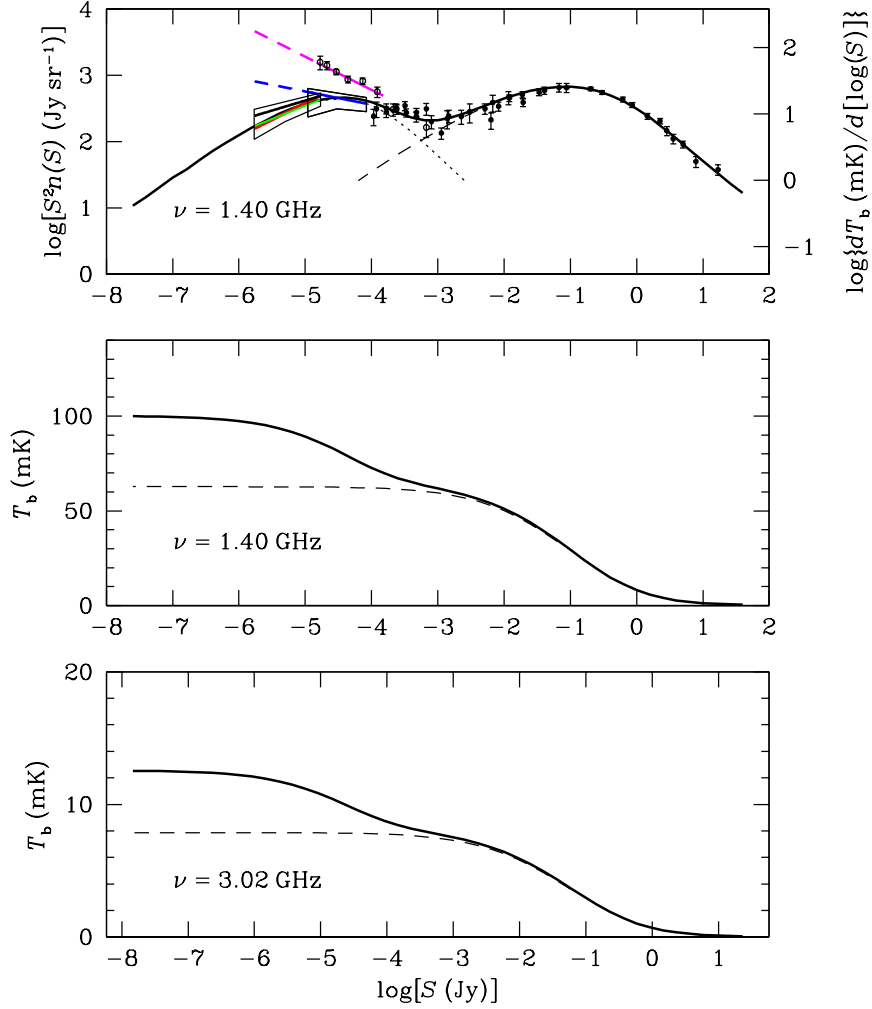


Figure 13. Brightness weighted source counts and model sky background temperatures at 1.4 and 3.02 GHz. The top panel shows the weighted 1.40 GHz source count $S^2n(S)$ (Jy sr $^{-1}$), the weighting that reflects the contribution of sources to the sky background temperature T_b per decade of flux density S . The plotted source counts at 1.40 GHz are based on individual sources (data points), the 1.4 GHz $P(D)$ distribution (blue line and surrounding error box) from Mitchell & Condon (1985), and our 3.02 GHz $P(D)$ distribution (black line and surrounding error box) converted to 1.40 GHz via a mean spectral index $\alpha = -0.7$. The red and green lines are power-law approximations to the 1.40 GHz models of Condon (1984b) and Wilman et al. (2008), respectively. The dashed curve is the contribution of AGNs and the dotted curve is the contribution of star-forming galaxies, from the Condon (1984b) model. Abscissa: log flux density (Jy). Ordinates, top panel: Log of the 1.40 GHz source count $S^2n(S)$ (Jy sr $^{-1}$) on the left, weighted to be proportional to the source contribution $dT_b/d[\log(S)]$ (mK) to the sky background per decade of flux density on the right. Ordinate, middle panel: Log of the 1.40 GHz sky background temperature (mK) contributed by all sources stronger than S at 1.40 GHz. Ordinate, bottom panel: 3.02 GHz sky background temperature (mK) contributed by all sources stronger than S at 3.02 GHz.

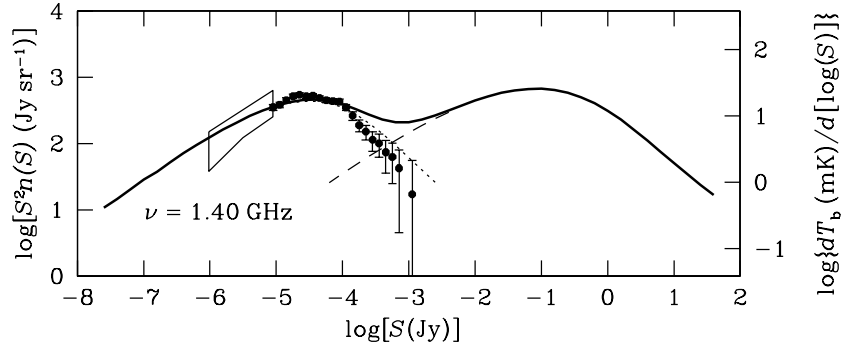


Figure 14. FIR source count converted to 1.4 GHz. The data points and $P(D)$ error box show the $\lambda = 160 \mu\text{m}$ FIR counts of Berta et al. (2011) converted to 1.4 GHz via the FIR/radio relation $\log[S(160 \mu\text{m})/S(1.4 \text{ GHz})] = 2.5$. The curves are predictions from the Condon (1984b) 1.4 GHz count model for star-forming galaxies (dots), AGNs (dashes), and their sum (continuous). The agreement with the actual 1.4 GHz counts shown in Figure 13 is within the errors. Abscissa: log of the 1.40 GHz source count $S^2n(S)$ (Jy sr^{-1}) on the left, weighted to be proportional to the source contribution $dT_b/d[\log(S)]$ (mK) to the sky background per decade of flux density on the right.

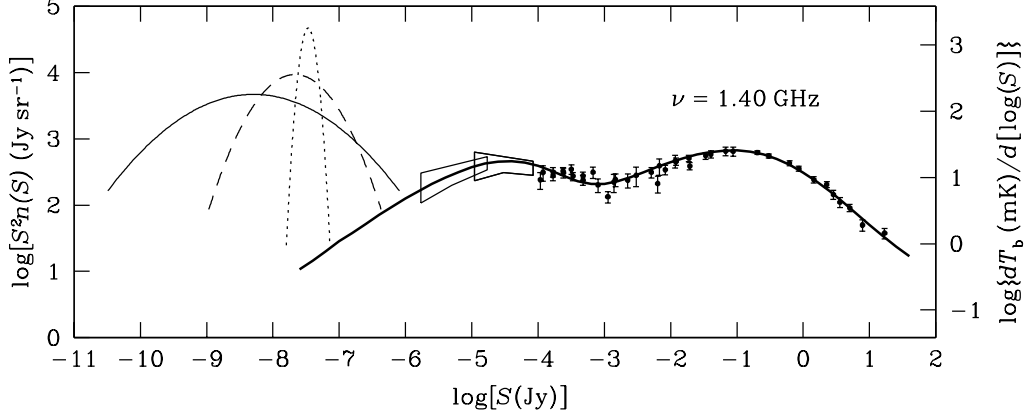


Figure 15. Source counts at 1.4 GHz consistent with the ARCADE2 background and our $P(D)$ distribution. Source counts at 1.40 GHz based on individual sources (data points), the 1.4 GHz $P(D)$ distribution (blue line and surrounding error box) from Mitchell & Condon (1985), and our 3.02 GHz $P(D)$ distribution (black line and surrounding error box) converted to 1.40 GHz via a mean spectral index $\alpha = -0.7$. The red and green lines are power-law approximations to the 1.40 GHz models of Condon (1984b) and Wilman et al. (2008), respectively. The dashed curve is the contribution of AGNs and the dotted curve is the contribution of star-forming galaxies, from the Condon (1984b) model. The three parabolas at nanoJy levels correspond to models for a hypothetical new population of radio sources able to produce the ARCADE2 excess background temperature. Their widths are $\phi = 0.2$ (dotted), 1.0 (dashed), and 2.0 (continuous curve), where ϕ is defined by equation 30. Our upper limit on the rms background fluctuation sets upper limits on the flux densities S_{pk} at the peaks of these parabolas and hence lower limits on the sky density of the new population. Even in the limit of a very narrow flux-density distribution, the number of sources per square arcmin is $N > 6 \times 10^4 \text{ arcmin}^{-2}$, which greatly exceeds the $N \sim 10^3 \text{ arcmin}^{-2}$ galaxies brighter than $m = +29$ in the Hubble Ultra Deep Field (HUDF). Abscissa: log 1.4 GHz flux density (Jy). Ordinates: log of the 1.40 GHz source count $S^2n(S)$ (Jy sr^{-1}) on the left, weighted to be proportional to the source contribution $dT_b/d[\log(S)]$ (mK) to the sky background per decade of flux density on the right.

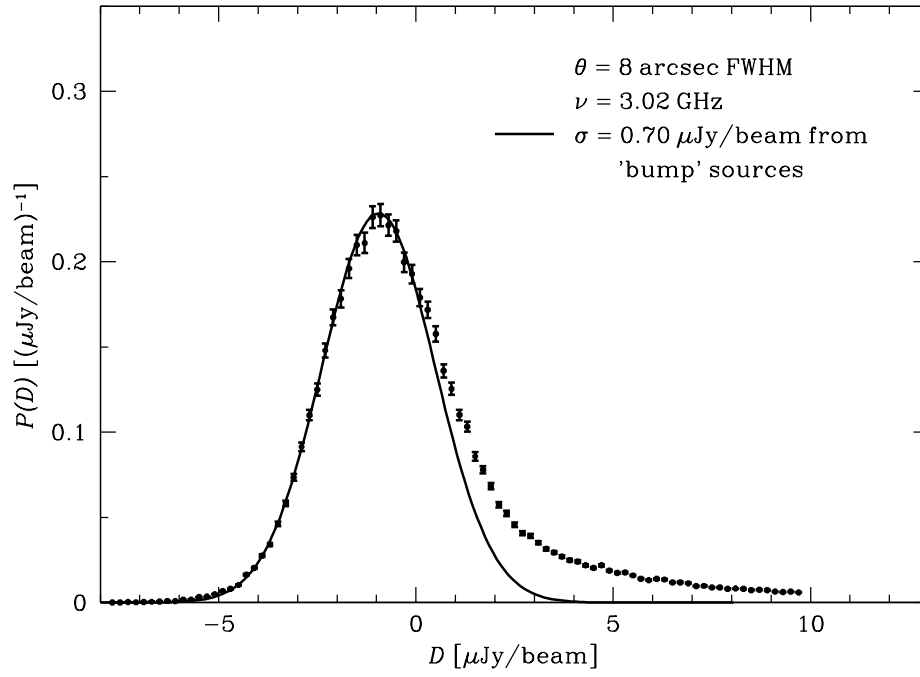


Figure 16. The largest possible contribution of numerous faint sources to the observed $P(D)$ distribution. A sharp “bump” in the number of extremely faint ($S \ll 1 \mu\text{Jy}$) faint sources would contribute a Gaussian to the observed 3.02 GHz $P(D)$ distribution. The rms of that Gaussian cannot exceed $\sigma \approx 0.70 \mu\text{Jy beam}^{-1}$ without excessively broadening our observed $P(D)$ distribution, no matter how low the source count near $S \sim 1 \mu\text{Jy}$. Abscissa: Deflection or peak flux density ($\mu\text{Jy/beam}$) at 3.02 GHz. Ordinate: Probability density ($\mu\text{Jy beam}^{-1}$).

Table 1
Subband Images

Subband number	Frequency (GHz)	S(3C 286) (Jy)	σ_n ($\mu\text{Jy beam}^{-1}$)
01	2.0500	12.260	9.220
02	2.1780	11.877	13.190
03	2.3060	11.522	18.170
04	2.4340	11.193	4.476
05	2.5620	10.885	4.244
06	2.6900	10.597	4.314
07	2.8180	10.327	4.039
08	2.9460	10.073	3.719
09	3.0500	9.877	4.477
10	3.1780	9.648	3.145
11	3.3060	9.432	3.067
12	3.4340	9.226	2.965
13	3.5620	9.031	2.882
14	3.6900	8.845	3.468
15	3.8180	8.668	4.447
16	3.9460	8.580	4.402